Simulation-Assisted Analysis and Design of Microfluidic Polymerase Chain Reaction Assay Devices

by

Nemanja Kliska

A thesis
presented to the University of Waterloo
in fulfilment of the
thesis requirement for the degree of
Master of Applied Science
in
Chemical Engineering

Waterloo, Ontario, Canada, 2015

I hereby declare that I am the sole author of this thesis. This is a true copy of the thesis, including any required final revisions, as accepted by my examiners.

I understand that my thesis may be made electronically available to the public.

Abstract

The Polymerase Chain Reaction (PCR) is a method by which sample DNA can be sequentially copied in order to increase the concentration of the sample DNA so that it can be measured directly. Interestingly, only specific DNA segments selected by the operator are amplified, if those segments are present in the sample then one will see DNA amplification otherwise nothing will be amplified. As a result, assays can be tailored to detect a wide range of disorders including bacterial infections, viral infections, and even genetic abnormalities/disorders.

PCR is a thermally actuated process where the chemistry is governed by the temperature of the reaction chamber. By adjusting the temperature of a PCR reactor through a set of three simple steps the concentration of target sample DNA is roughly doubled at the end of each cycle. However, the reactants are very temperature sensitive. As a result precise temperature control is required in order to conduct a successful PCR run.

With the advent of microfluidics, PCR has been miniaturized onto lab-on-chip systems. These systems have many advantages over their conventional counterparts (laboratory scale biological assay with bench-top thermal cycling systems) such as reduced cycling times and reduced reagent costs due to smaller sample volumes, increased automation due to on-chip integration with other modules (for other process steps), and reduced power consumption due to better integration with heating systems. However, the design of these microfluidic systems also has its unique challenges. High thermal gradients throughout the system are commonplace; as a result it is difficult to ensure thermal uniformity within the reaction chamber. Furthermore, it is difficult to correlate the measured temperature of external temperature probes with the temperature of the reactor itself. Lastly, it is very difficult to experimentally measure the real-time temperature profile of the PCR chamber, since any sensor perturbs the system greatly.

The work presented within this report will focus on the thermal design of typical microfluidic PCR reactors. Our analysis is focused on using simulation-aided-design to offer insights that serve to validate and optimize the performance of these exemplary reactors. In order to do this, we modified `OpenFOAM`, an open-source CFD simulation suite that relies on the Finite Volume Method, to include a heat generation term as well as PID control. We first focused on running transient simulation in the absence of control in order to optimize the physical design of our example reactor. Subsequently, we investigated the effect of feedback control on the sample system in order to validate the results obtained experimentally. In order to do this we emulated the entire experimental system and matched the control scheme/parameters used experimentally.

What we found was that our simulations were able to provide insights that were otherwise unobtainable. We were able to map the full 3D temperature field of the system in a high fidelity transient simulation. Using this data, we determined that placement of the temperature sensor was crucial to the performance of the device. Furthermore, we discovered that manifold layers relatively far away from the reactor chamber had a profound effect on the temperature measured by out temperature sensor. As a result, the design was modified to include an additional heat spreading layer so that the measured temperature would better reflect the temperature of the chamber. Moreover, our open loop simulations illustrated that simple 1D analytical models were not adequate to predict the performance of microfluidic PCR systems.

Our second set of simulations focused on studying how PID control affects the temperature profile of the system over time. Originally experimental validation was done on the optimized system. It was found that the design did not successfully amplify the target DNA sequence, likely due to the amplification of primer-dimers. Using our simulation methodology analysis we found that the heating/cooling rate of the system was position dependent. In our specific example, our temperature sensor was closer to the heating element; thus reaching target temperature well before the reactor itself. Our simulations identified transient discrepancy between the measured temperature and the reactor temperature. Using this information we were able to adjust the control scheme of the experimental system which resulted in successful amplification.

Overall the simulation-aided-design exercise has been invaluable in troubleshooting and optimizing the design of microfluidic PCR devices.

Acknowledgements

First and foremost I would like to acknowledge my co-supervisors: Dr. Nasser Abukhdeir and Dr. Chris Backhouse. Their mentoring and support have been invaluable throughout my Master's program.

Furthermore, I would like to acknowledge all of my colleagues from the Abukhdeir research group: Tanytakarn Treeratanaphitak, Grigoriy Kimaev, Pendar Mahmoudi, Yining Han, and Amir Mowla for their support throughout my Master's. I would also like to thank my fellow colleagues from the AML research group: Gordon Hall and Tianchi Ma for there tireless work in conducting the experimental analysis described here in.

Additionally, I would like to thank Dr. Moira Glerum for all of her help with our paper. Moreover, I would like to thank Austin Boucinha for his tireless work with the various simulations we worked on together.

Finally, I would like to thank my family for supporting me through this endeavour.

Table of Contents

List of Tables

List of Figures

xi

Chapter 1

Introduction

Diagnostic techniques for infectious diseases are fundamental in modern medicine. Various approaches exist for the diagnosis of infectious diseases [28,64] and typically involve remote and costly laboratory-based analysis and long turnaround times. Advances that address these issues, especially reduction of cost and turnaround time, would have significant positive impact throughout the world. Traditional diagnostic techniques for infectious diseases include [28,64]:

Cell Culturing or *in vitro* cultivation is the process by which cells are grown outside of their natural environment in a controlled laboratory setting. To this day it remains the standard diagnostic technique for infectious diseases and involves the use of cells sampled from the patient. Cell culturing is expensive in that it requires laboratory facilities,relatively large supplies of consumables, and highly-trained staff [64]. The advantages of cell culturing are that its sensitive, specific, and it has the ability to be simultaneously determine the antibiotic susceptibility for certain microbes. However, in some cases target microbes require special culturing media and conditions which further complicates the cell culturing process. In many cases the cell culturing processes expose laboratory technicians to health hazards due to the amplification of disease-causing microbes. Finally, successful cultivation does not necessarily lead to a successful diagnosis. Typically, diagnosis is performed through phenotypic tests (tests where microbial colonies are grown under different laboratory conditions designed to differentiate strains and species based on the characteristics of known microbes) which have limited discriminatory power due to varying states of the sample microbe [28].

Serology diagnosis techniques involve analysis of the plasma serum and/or other bodily fluids of a patient to determine if specific sets of antibodies are present indicating the

existence of a microbial infection. As with cell culturing, serology requires laboratory facilities and technicians to be performed. Also like cell culturing, experiments can be developed to identify specific viral and bacterial strains. However, these experiments may still fail to identify the correct pathogen if host cells succumb to the infection prior to mounting an immunological response [28].

Microscopy is the least used traditional diagnostic technique in that it relies on visual identification of microbes in patient samples. In general, this technique is less reliable than other standard techniques and requires large concentrations of microbes to be present in samples ($\approx 10^4$ bacteria per millilitre). In order to identify a pathogen, specific dyes are used that illuminate specific microbes. Then, a trained microscopist must search through the sample and determine whether or not there is anything present. This method relies heavily on dye selection as well as the capabilities of the microscopist, and as a result, it is most prone to error of all the conventional methods [28].

A "next-generation" alternative technique to traditional methods is *nuclear sequencing* which involves analysis of the genome of a biological sample through DNA sequencing in order to identify target pathogens. Nuclear sequencing approaches, specifically the polymerase chain reaction (PCR) method, have significant advantages compared to traditional techniques. They are inherently more safe in that biological samples are lysed and thus pathogens are inactive but their DNA is preserved [28]. Additionally, the PCR method both requires less time and is more sensitive than traditional techniques including cell culturing [28]. Thus far smaller biological samples are required; PCR amplifications of single DNA molecule have been carried out in a research environment [88]. Finally, PCR is a lower cost diagnosis technique due to its ability to be automated and to its overall simplicity [64].

1.1 The Polymerase Chain Reaction (PCR) Assay

The PCR assay is a genetic assay that amplifies a individual DNA molecules through the repetition of a series of *amplification cycles*. Following a successful PCR cycle, the number of target DNA molecules is approximately doubled. In order to achieve this amplification, the PCR assay relies on a set of three thermally-actuated reaction steps (Figure 1.1): denaturation, annealing, and extension (for a more complete description of PCR please refer to Chapter 2).
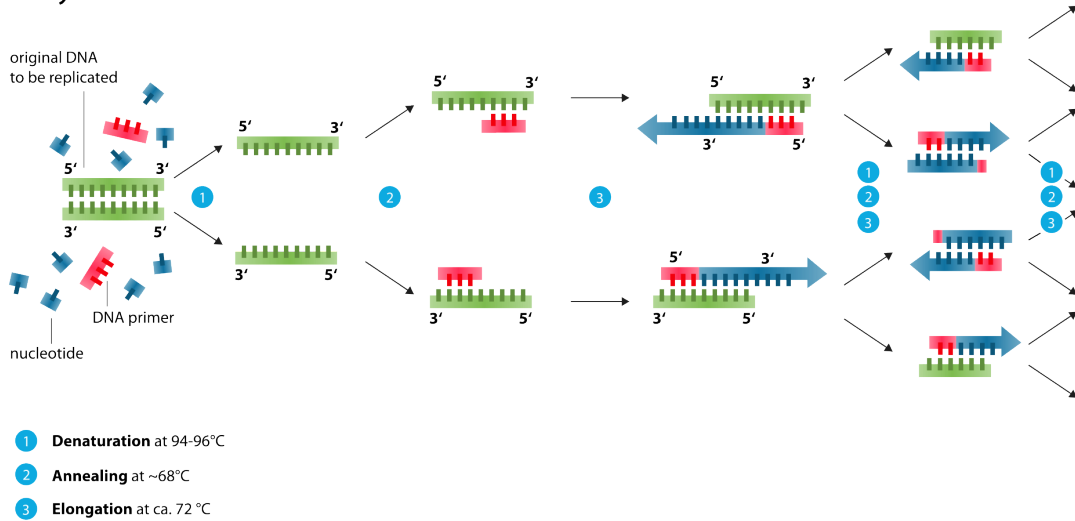
Figure 1.1: Schematic representation of the PCR assay. Image taken from ref. [20].

Denaturation or melting involves raising the temperature of the sample above melting point of DNA ($95°C$); above this temperature the two strands of DNA become separated in solution.

Annealing following denaturation the sample is cooled to approximately $55°C$ at which the individual DNA strands interact and complex with other reactants in solution. These additional reactants are called *primers* and have a chemical composition such that they match the beginning ("sense" primer) and end ("anti-sense") of the target DNA sequence to be amplified. The annealing temperature is dependent on the chemical composition of the specific primer reactants. In practice the annealing temperature is approximately $\approx 55°C$ or greater.

Extension is the final cycle of the PCR assay and involves heating of the reaction chamber in order to activate a third reaction component, a biological enzyme which catalyzes polymerization, or a polymerase. A DNA polymerase is a catalytic enzyme that promotes the addition of new nucleotides to the 3' end of an existing strand of DNA. In this stage the target DNA sequence is copied and it is also known as the *elongation* stage. An example of a polymerase used in this stage is Taq polymerase [11] which is thermally activated, where the peak catalytic activity is found at approximately $80°C$.

3

As previously mentioned, the simplicity of the PCR assay has led to the development and application of automated bench-top PCR systems for genetic assay-based disease diagnosis. An example of a conventional system is depicted in Figure 1.2a. While these desktop PCR systems have significant advantages over traditional diagnostic techniques, they still require laboratory facilities and relatively large amounts of consumables. The miniaturization of PCR devices to the micro- and nano-scales would further increase the desirability of this next-generation diagnostic technique. Decreasing PCR reaction chamber size results in the need for even smaller biological samples, the consumption of less reagents, and a decrease in diagnosis time. Significant work has been done towards development of microfluidic PCR devices and integrated lab-on-a-chip devices which include the PCR assay as one possible functionality. An example of a microfluidic PCR device shown in Figure 1.2b.

| (a) | (b) |
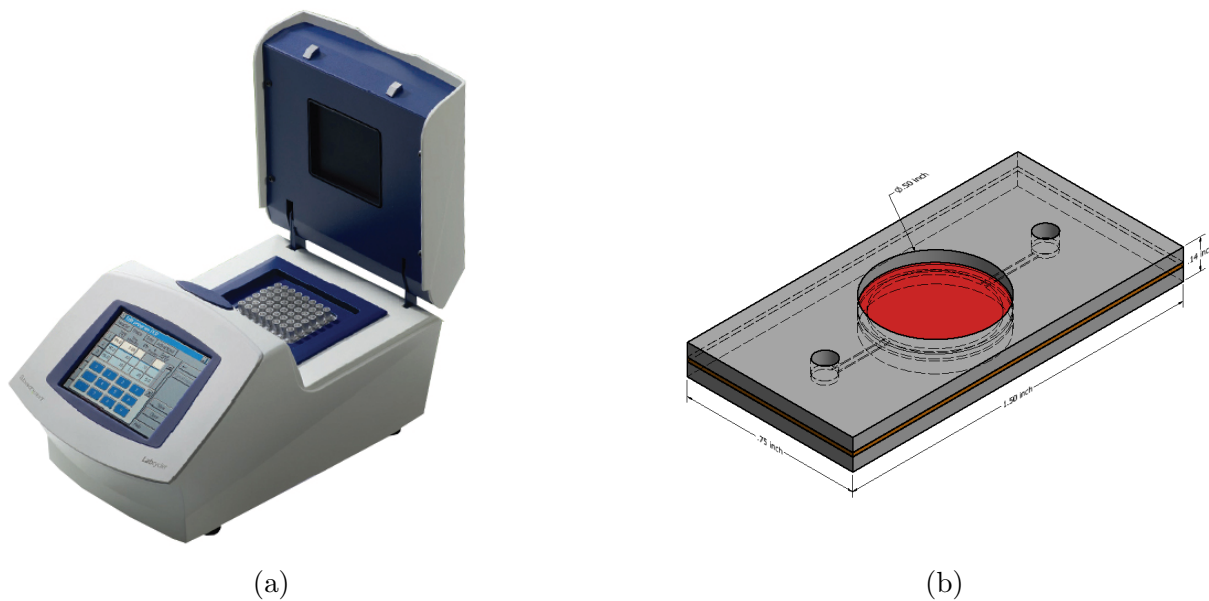
Figure 1.2: Examples of (a) a conventional [71] and (b) a microfluidic PCR device.

1.2 Objectives

The overall objective of this research project is to use simulation-based engineering to aid in the analysis and optimization of existing microfluidic PCR designs and enable the design of "clean-sheet" designs which could be easily integrated into lab-on-chip technologies.

Robust simulation software exists which is able to perform heat transfer analysis on devices with multiple sub-domains and phases (solid, liquid, and gas). The `OpenFOAM` finite-volume method library is used in this work perform heat transfer analysis simulations for analysis, optimization, and design tasks. Furthermore, experimental analysis simulated microfluidic PCR devices was performed through collaborations with the Backhouse group (UW).

Specific objectives of this research project are to:

1. Implement and validate of an in-house `OpenFOAM`-based conjugate heat transfer solver which includes microfluidic PCR-specific functionality such as bulk heating and P&ID control.

2. Simulate an existing prototype microfluidic PCR device to predict transient temperature profiles within the PCR reaction chamber and effectiveness of experimentally-designed control schemes.

3. Determine qualitative relationships between PCR chamber conditions and PCR reaction efficiency through analysis of electropherogram measurements of the experimental device reaction products and simulation predictions of reaction chamber conditions.

4. Determine insights from simulation predictions of device performance (reaction chamber temperature uniformity and control effectiveness) for future design optimizations and "clean-sheet" re-designs of microfluidic PCR devices.

Chapter 2

Background

2.1 The Polymerase Chain Reaction (PCR) Assay

The polymerase chain reaction (PCR) assay is the most mature and well-adopted DNA amplification method due to its simplicity [64]. Nuclear amplification in biology refers to increasing the number density of target DNA molecules of a specified sequence. PCR achieves this through the repetition of successive amplification cycles using selective reactants for a desired DNA sequence, or target sequence.

The PCR assay is essentially a sequence of chemical reactions that involve six basic reactants: DNA (or RNA), two types of DNA "primer" molecules, a DNA polymerase, nucleotides (DNA building blocks), and a solvent (water). The sample DNA (or RNA) is extracted from a biological sample that is to be tested. The PCR amplification process is specific to short sequences which are indicative of a disease being present (infectious or genetic). This specificity is achieved through the use of a set of DNA "primers", small oligonucleotides consisting of a precise sequence of 18-24 base DNA pairs. These primers are extended/replicated during the PCR process if complementary sequences are present in the sample DNA [49]. The double-stranded structure of DNA requires the use of paired DNA primers molecules: forward ("sense") and reverse ("anti-sense") primers. The forward and reverse primers bind to sense and anti-sense DNA strands respectively, and form hybridized DNA molecules. The DNA polymerase component of the mixture then acts as a catalyst for a complex series of reactions that extend both DNA primer molecules to match the target sequence from the sample DNA. This reaction process requires an additional component to be present in the mixture, nucleotides (DNA building blocks).

This reaction sequence is called a PCR cycle and involves three thermally-actuated stages [28]: denaturation, annealing, and extension. A schematic of this process is shown in Figure 1.1. In summary, the denaturation step "melts" the target DNA from a single composite strand into a pair of single strands. Following denaturation, the annealing stage involves cooling the sample DNA, which is now decomposed into single stranded molecules, to a temperature at which the single strands hybridize with PCR primers if the target DNA sequence is present. Finally, the extension stage involves heating the reactor to a temperature at which the polymerase becomes active and replicates the target DNA sequence through acting on the DNA/primer hybridized molecules(if present). This sequence of stages have complex couplings which result in engineering issues associated with heating and cooling rates and holding times.

2.1.1 Denaturation Stage

During the denaturation stage the PCR reaction chamber is heated above the melting temperature of the sample DNA. Typically, long strands of DNA have a melting point of $\approx 95°C$ depending on ion concentration in the buffer solution and the percentage of GC pairs (this refers percentage of hydrogen bonds between Guanine and Cytosine nucleotides as opposed the percentage of Thymine and Adenine interactions) in the sample sequence. An empirical expression for the melting point T_m (Celsius) for double helix DNA has been determined [81]:

$$T_m = 77.1 + 11.7 log[Na^+_{eq}] + 0.41(\%GC) - \frac{528}{N_{bp}} - 0.75(\%DMSO) \qquad (2.1)$$

where $[Na^+_{eq}]$ is the effective ion concentration in mol/L, $\%GC$ is the percentage of GC base pairs in the sample sequence, N_{bp} is the number of base pairs in the sample, and $\%DMSO$ is the percentage of DMSO solvent (the volumetric percentage of DMSO in a solution of water and DMSO) used in the reaction chamber [81]. The effective ion concentration ($[Na^+_{eq}]$) is found through the following equation [81]:

$$[Na^+_{eq}] = [\text{Monovalent Cations}] + 120\sqrt{[Mg^{2+}] - [dNTPs]} \qquad (2.2)$$

where $[Mg^{2+}]$ is the concentration of magnesium ions in solution, $[dNTPs]$ is the concentration of deoxynucleotide triphosphates present, and all concentrations are given in $mmol/L$ for equation 2.2.

Achieving a suitable melting temperature is critical for PCR reaction effectiveness in that if the reaction chamber is too low then fewer DNA molecules will disassociate. This

negatively affects the efficiency of amplification in subsequent stages. Alternately, the higher the reactor chamber temperature the greater the degree of polymerase molecule degradation. For example, Taq polymerase has been found to noticably degrade at temperatures of 95°C and greater [49]. An enzyme's catalytic properties are strongly tied to its shape; as a result, exposure to 95°C the Taq polymerase species has a half-life of $40 - 50min$ [49]. At 97.5°C the half-life decreases to $\approx 9min$. Figure 2.1 show catalytic activity versus time at three different temperatures for Taq [49].
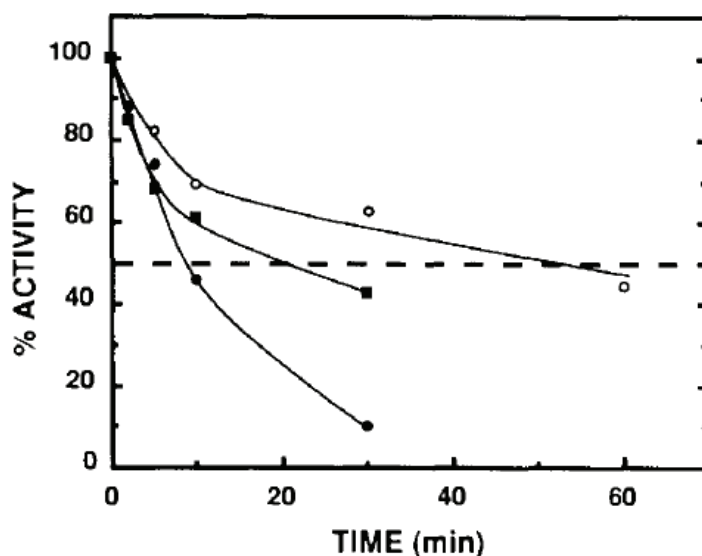
Figure 2.1: Taq Polymerase Activity as a Function of Time Exposed to a Particular Temperature, (●) Taq polymerase at 97.5°C, (○) Taq Polymerase at 95°C [49]

Typically about 30 PCR cycles used to amplify the orginal DNA segment [88], precise temperature control during the denaturation stage and short hold times are crucial to long term polymerase viability.

2.1.2 Annealing Stage

Following the denaturation stage the sample DNA is single-stranded. The annealing stage is initiated by rapid cooling of the reaction chamber. At lower temperatures complexes of DNA primers and single strand DNA molecules form if target sequences are present in the sample. Concurrently, complementary pairs of single strand DNA molecules are able to

reform compound DNA molecules. Typically the concentration of DNA primers is at least 10^9 greater than the initial concentration of the sample DNA in order to bias the reaction kinetics toward DNA/DNA primer hybridization. The hold time for the annealing stage is determined based upon the characteristic time associated with DNA strand diffusion in the buffer solution. The average distance between two single strand DNA molecules at the end of the annealing stage, assuming an initially perfectly mixed solution, is:

$$d \gg \sqrt{Dt} \qquad (2.3)$$

where d is the average spacing between two sample DNA molecules, D is the diffusion constant of DNA in the buffer solution, and t is the annealing time.

In addition to controlling hold time during the annealing stage, the temperature at which the reaction chamber is held has an effect on the efficiency and specificity of the hybridization reaction. There exists an optimum annealing temperature (T_a^{OPT}) at which amplification efficiency is maximized while non-specific amplification products are minimized. Non-specific amplification occurs when primers bind to unintended binding sites (i.e. two primers bind to one another). During subsequent extension steps these sites are amplified.

It has been proposed that this optimal temperature may be derived as the weighted average of the melting temperatures of the primer (T_m^{primer}) and the amplification product ($T_m^{product}$). An empirical relationship that estimates this optimum temperature is given by [65]:

$$T_a^{OPT} = 0.3T_m^{primer} + 0.7T_m^{product} - 14.9°C \qquad (2.4)$$

If the annealing temperature is too low, the primers will be more likely to bind to sites other than the target site on the sample, resulting in the production of more non-specific amplification in subsequent extension stages. For example primers may instead hybridize with other partially complimentary primer to form hybridized primer pairs. During the extension stage, these primers will produce primer-dimer structures where unhybridized regions of the original primers will be seeded with nucleotides complementary to the other hybridized primer. Once this happens, these structures cannot be used to replicate the target sequence.

On the other hand if the annealing temperature is too high, it is more energetically favourable for the primers to remain in solution. As a result, during subsequent extension stages there are fewer primers present for amplification to occur [65].

2.1.3 Extension Stage

Following the annealing stage, the majority of single stranded DNA molecules that have the target DNA sequence present are hybridized with the respective DNA primer. The reaction chamber temperature is then raised to activate the polymerase molecules in order to make a copy of the target DNA sequence using each of the DNA primers present in the newly hybridized DNA molecule. The single strand DNA is used as a template by the polymerase which binds nucleotides in solution from solution sequentially onto the end DNA primer (as part of the hybridized molecule). Since the primer and sample have been hybridized during the previous annealing phase, new nucleotides added to the primer must be complementary to those present in the original sample. Given that there exist two complementary single strand DNA molecules for each of the initial double strand molecules, the final stage of the PCR assay copies/amplifies *both* the forward and reverse primers to produce two complementary strands that mirror the target sequence of the sample DNA.

During the extension stage, the key design constraint is maximizing polymerase activity. Taq polymerase, for example, is active over a narrow temperature range [11] as shown in Figure 2.2. Peak Taq catalytic activity is found at approximately $80°C$ and thus precise temperature control about this set-point will enable the minimization of the extension stage.
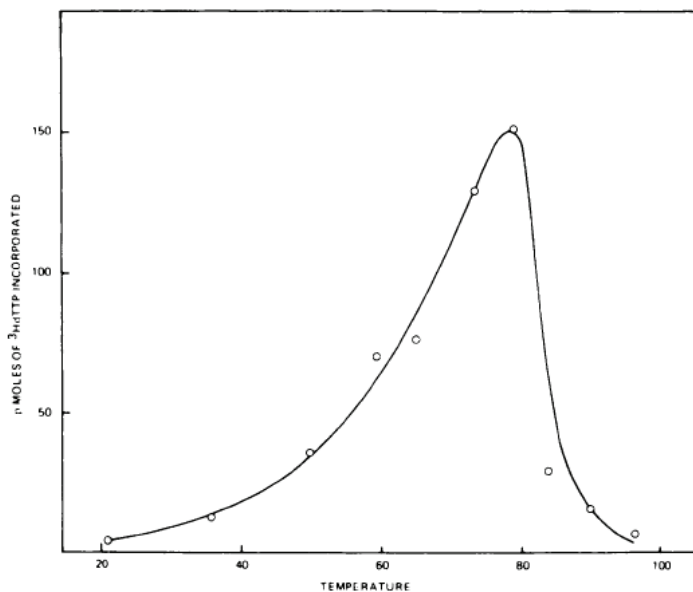
Figure 2.2: Effect of temperature on the activity of Taq polymerase activity [11].

10

2.2 Microfluidic Devices

Since their first development PCR reactors have been shrinking. Currently, the state-of-the-art of PCR devices are both microfluidic-based and involve integration of the PCR assay with genetic characterization functionality. Miniaturizing PCR devices into a microfluidic device can reduce analysis time, reduce system/operational complexity, reduce operational costs by minimizing reagent volume, and reduce the overall cost of such a system to the point where it is disposable [64, 88]. These "total" analysis systems are poised to replace conventional bench-top devices for medical diagnoses and, ultimately, enable point-of-care diagnosis.

Since they were first introduced in the early 1990's, two general types of microfluidic PCR reactors have been developed:

Stationary Chamber Reactors PCR reactors use sealed reaction chambers where heating elements heat and cool the PCR mixture. In order to complete a full PCR run, the seal chamber must cycle through each of the three stages of the PCR assay.

Flow-through Reactors PCR reactors use flow of the PCR mixture through microfluidic channels which create a pathway through spatial zones of the device which are maintained a each of the three temperatures required for the PCR assay.

2.2.1 Stationary Chamber PCR Reactors

In 1993 Northrop et al. created the first micro-fabricated PCR reactor [59]. They implemented two systems with varying reactor volumes ($25\mu L$ and $50\mu L$ reactors). Figure 2.3 below depicts a cross-section exemplary system. The main portion of the reactor was constructed from a silicon wafer where a well was etched out using lithographic techniques. The chamber was sealed using a silicon nitride membrane which was attached to a polysilicon thin film heating element . In their design the heating element was also used to measure/control temperature through an empirical relationship between average heater temperature and its resistance. Using this setup with closed-loop control they were able to heat/cool at a maximum rate of $13°C/s$ and $35°C/s$ respectively [59].

One of the main challenges with these designs has been temperature control. In addition to the reaction chamber, the surrounds of the device must be heated and cooled in order to maintain temperature uniformity in the PCR chamber. Frequently flow and construction design constraints result in sub-optimal thermal properties. As a result, the
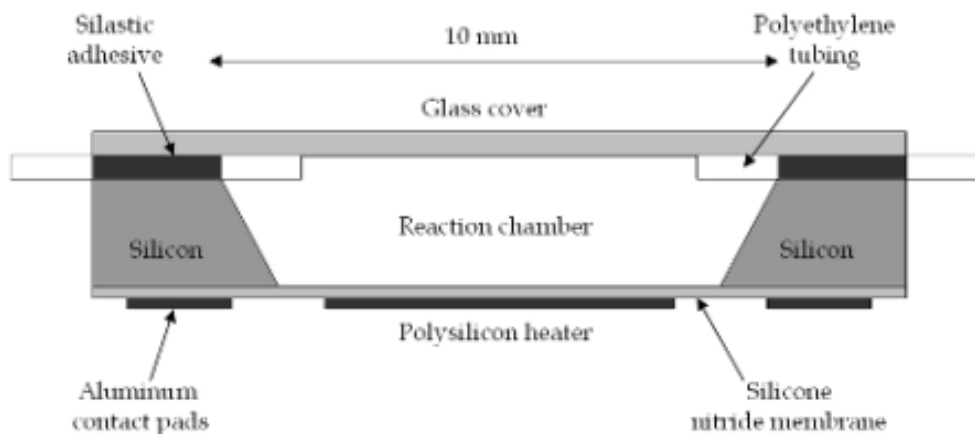
Figure 2.3: Schematic cross section of the single chamber stationary PCR reactor developed by Northrop et al [59]. Figure taken from ref. [68].

thermal characteristics of both the solid and liquid layer must be accounted for in a given design. Additionally, while smaller reactor volumes are good for small sample diagnosis, they have low total throughput. Therefore, stationary single chamber systems are usually slower than their flow-through counterparts.

Since this first advance there have been many permutations to the initial design [1, 7, 8, 10, 16, 19, 21–23, 25, 26, 33, 34, 36, 39, 40, 44, 45, 47, 48, 50, 52, 59, 72, 73, 85, 91]. Most of this research has focused on improving the integration of PCR reactors with upstream and downstream microfluidic processing modules. For example, electrophoresis modules are frequently integrated downstream of the PCR module in order to analyze the amplified genetic output. Extending these systems to sequence and copy other biological samples such as RNA using RT(Reverse Transcriptase)-PCR. Yet other groups have focused on improving the operating efficiency of these devices by improving cycling speed and reducing power consumption.

One of the most significant areas of research have involved fabricating PCR devices out of less expensive and biocompatible materials. First-generation PCR reactors were etched into silicon wafers which involved costly fabrication processes and were not biocompatible.

New fabrication techniques have typically used lithography of some form, ranging from etching glass to different types of polymers and plastics. Additionally, micromachining has also been used. Thin film plastic-based devices are typically the least difficult to manufacture and are of interest for disposable point-of-care devices. One of the main drawbacks of these systems in slower cycle times compared to their silicon-based counterparts due to the lower thermal conductivity of polymers (as compared with glass or silicon).

One approach to address the low throughput characteristic of stationary chamber PCR devices has been through the addition of many chambers to a single device. These multi-chamber stationary PCR devices [9, 16–18, 29, 41, 51, 53, 54, 56–58, 74, 76, 77, 79, 82, 86, 87, 89, 92, 93] are essentially an extension of their single chamber counterparts and have been investigated by a multitude of research groups. Using this method many PCR amplifications can be done in parallel thus improving the processing time for complex analyses where multiple markers may be targeted. The main drawbacks to these devices are that the additional complexity of the multiple chambers and supporting microfluidic exacerbates the temperature control and variation issues.

2.2.2 Flow-through PCR Reactors

The second main type of microfluidic PCR device is the *flow-through* type where the PCR mixture flows through successive temperature zones which result in the required PCR temperature cycle as in conventional PCR. Thus there is a continuous variation in the PCR sequence for each control volume of the mixture as a function of the residence time within the reactor. In order to simplify the hydrodynamic aspect of the design these reactors are typically operated in the plug flow regime which also minimizes cross-contamination of sequential samples through axial diffusion.

Flow-through PCR reactors sacrifice complexity of the initial design for simplicity of temperature control. Each spatial region of the PCR device may be kept at a uniform temperature and its size and relationship to other zones configured to enable the PCR cycle through convection of the PCR mixture through the reactor. Each zone is relatively large with respect to the volume of the microfluidic channel passing through it and thus conductive heat transfer dominates so that the incoming PCR mixture rapidly reaches thermal equilibrium within the zone. This allows for simple open loop control in many cases.

This type of design does have several disadvantages. The number of PCR cycles is fixed at the design stage and requires precise control of volumetric flow through the device. As a result, each design must be designed custom to the particular PCR analysis.

13

Flow-through reactor designs can be subdivided into three broad categories.

Capillary flow-through PCR reactors are one of the most simple implementations of flow-through reactors [4, 6, 12] in that they are composed of a capillary tube in place of a microfluidic chip. The capillary is position across three heating blocks of various size which are maintained at the three different PCR cycle temperature for the desired analysis. Using this approach Chiou et al. developed a PCR reactor that could achieve 78% (yield of amplification over the theoretical amplification limit) in 23 minutes [12]. Their implementation is depicted in the figure 2.4a.

Serpentine flow-through PCR reactors use microfluidic channels which double-back on themselves [13, 24, 30–32, 46, 60, 61, 66, 67, 69, 70, 75, 90]. A single channel "snakes" back and forth across a set of steady heated zones at a constant rate as shown in Figure 2.4b. However, due to the arrangement of the device, the PCR fluid is exposed to a non-ideal PCR cycle: denaturation, extension (first), annealing, and extension (second). As a result, it is possible that the sample DNA hybridizes with complementary sample DNA fragments (undesired), in addition to DNA primers (desired), during the first extension stage resulting in reduced amplification efficiency.

The first serpentine reactor was developed by Kopp et al. in 1998, and is shown in Figure 2.4b. The reactor channel passed through the temperature zones 20 times using pressure driven flow. Overall amplification time ranged from $1.5 - 18.8min$ for flowrates of $72.9 - 5.8nL/s$, respectively. In this system high flow rates could be achieved due to the low transition times between adjacent temperature zones $(100ms)$ [46].

Circular flow-through PCR reactors use a simple circular channel which allows for more flexibility with respect to the number of PCR cycles that can be specified [15, 53, 63, 84]. Here the PCR fluid passes through the three PCR stages in an optimal sequence: denaturation, annealing, and then extension. This is achieved through a radial arrangement of heating elements and a spiral configuration of a single microfluidic channel or single closed loop.

2.3   Simulation in Microfluidics

Traditionally, PCR device research has relied on experimental methods to evaluate the performance of PCR devices. Direct experimentation is both costly and time-consuming

(a)

(b)
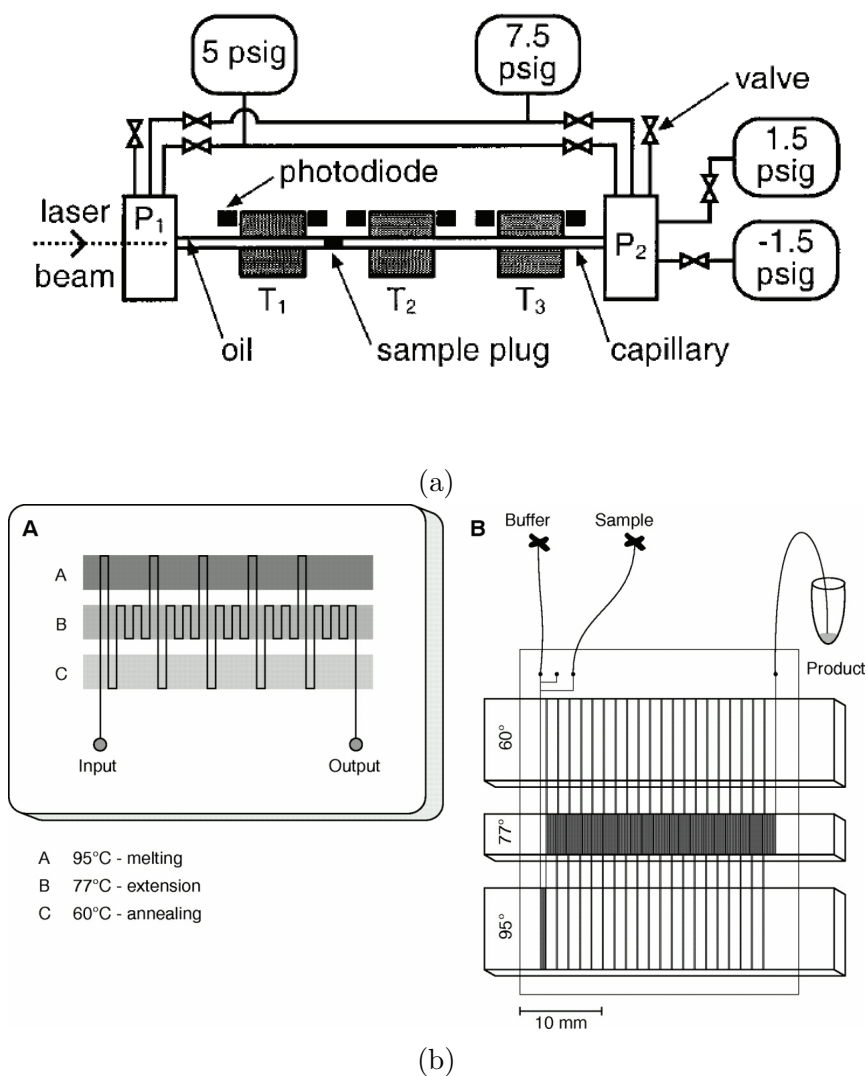
Figure 2.4: Schematic cross-sections of (a) capillary and (b) serpentine flow-through PCR reactors. Images were taken from refs. [12, 46], respectively

which has motivated the used of modelling and simulation. Two different types of theoretical approaches have been employed in the past: simple analytical solutions of simplified one-dimensional PCR designs and simulation-aided design using numerical solutions of governing heat transfer equations.

Simulation-assisted design of microfluidic PCR devices has the potential to significantly reduce the amount of experimental research required to achieve a functional and optimized microfluidic PCR device. Challenges do exist in simulating microfluidic PCR devices due to the coupled hydrodynamics, heat transfer, mass transfer, and reaction kinetics. Past studies have simplified this task by focusing on heat transfer in the presence of well-developed flow, but few of these studies have been able to achieve high-fidelity simulations of actual prototype designs.

2.3.1 Lumped Capacitance Analysis

Direct analytical solutions of heat transfer equations for simplified one-dimensional PCR designs can be relatively challenging due to the multiple domains and heat generation present in these systems. Approximate methods are typically used such as *lumped capacitance models* [9,16,41,83] which involves the assumption that the heat transfer is restricted to a linear path through the domain(s). This approach uses a linear circuit analog to decompose and discretize a given design into a finite number of components represented as a circuit. In this circuit, temperature is analogous to voltage and heat flow from one component to another is analogous to electric current. This representation is exact for an idealized one-dimensional system.

An example of an equivalent circuit for a steady state system is shown below in figure 2.5. Each component also features a resistance and capacitance where they are related to the thermal conductivity and specific capacity respectively for a given component.

Finally, the thermal mass (capacitance analog) is the amount of energy required to raise the temperature of a given component. With lumped capacitance, the standard procedure is to sum up the total thermal mass for each component.

Alternatively, a more complicated version of this model is referred to as the distributed capacitance model [3,43]. The added complexity arises from the placement of 'capacitors' alongside the 'resistors' in the original circuit. Unlike the lumped case, these circuits usually require a numerical solver. In the lumped case, an equivalent total thermal resistance is calculated based on the given circuit. This is used in conjunction with the total thermal mass, described above, to determine an approximate time constant. With lumped capacitance, it is assumed that the circuit can be simplified as shown below in figure 2.6. Under this assumption, the time constant (τ) can be calculated as shown in 2.5, where the temperature at some point of interest follows an exponential decay as shown in equation 2.6.

16
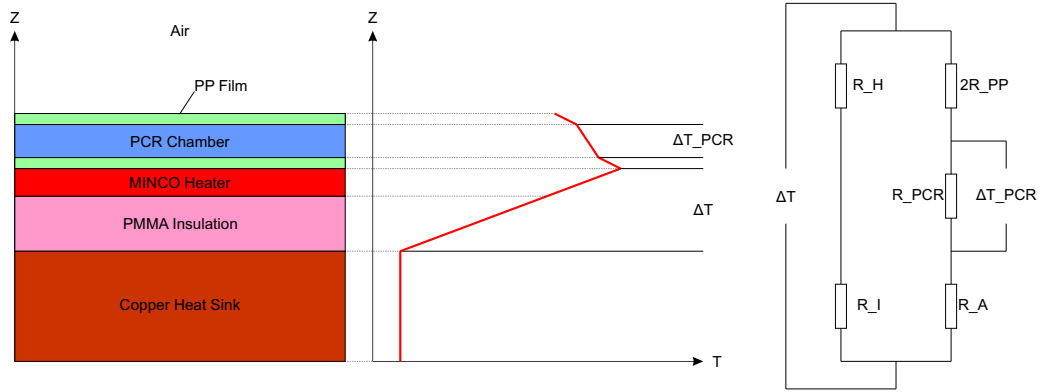
Figure 2.5: Example of an equivalent circuit to a 1D heat diffusion problem using the lumped capacitance approach
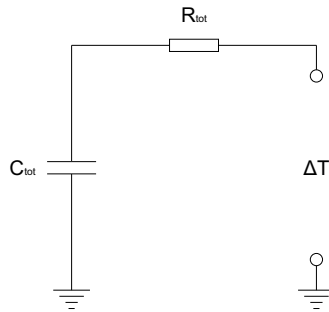
Figure 2.6: Simplified RC circuit used to calculate the approximate time constant of the system using the lumped capacitance method

$$\tau = R_{tot}C_{tot} \tag{2.5}$$

$$\frac{T(t) - T_i}{T_f - T_i} = 1 - e^{-\frac{t}{\tau}} \tag{2.6}$$

17

Lumped capacitance models are simple models mostly used as initial exploratory models for "roughing-out" an initial design. This heat transfer analysis method may be used to estimate the order of magnitude of the dynamic response of a given design, but the assumptions involved rapidly breakdown for even slightly complex geometries.

2.4   The Finite Volume Method

The finite-volume method is a frequently-used numerical method for direct solution of the partial differential equations involved in heat transfer analysis [14, 80]. The use of such a numerical method to solve governing continuum mechanics equations enables high-fidelity simulation of PCR microfluidic devices. The cost incurred for higher accuracy (as compared to analytical models) is a significant increase in the complexity of configuring, running, and interpreting simulation results. Like the finite element method, the finite volume method relies on the method of weighted residuals to discretize the spatial domain. Unlike finite element which uses the Galerkin method, the finite volume method uses the subdomain method. There are two major advantages to this approach, the first being that this is less computationally intensive since the weighting function is simpler. Secondly, for divergence terms the finite volume method is conservative.

Several software packages exist to simplify this task, one of which is open-source and open-access, the `OpenFOAM` library [78]. `OpenFOAM` implements the cell-centered finite volume method [42] and has a variety of developed solver applications for different types of applications of continuum mechanics. In this work we used conjugate heat transfer solver `chtMultiRegionFoam`, which solves the energy equation in both liquid and fluid regions with flow.

2.4.1   Method of Weighted Residuals

At its core the Finite Volume Method relies on the method of weighted residuals to discretize the spatial component of our governing equations. Consider the governing equation described in equation 2.7 where ϕ is our dependent variable, Su is a constant explicit source term, and ρ and Γ are constant parameters. One should note, that equation 2.7 takes the same form as the heat equation used in our simulation (equation 3.1). The following sections will describe how the heat equation is treated numerically in our solver.

$$\frac{\partial}{\partial t}\rho\phi - \nabla \cdot (\Gamma\nabla\phi) - Su = 0 \tag{2.7}$$

18

First let's define some arbitrary trial function $\phi'(\mathbf{x}, t)$which we will substitute into our governing equation. Since this is not the exact solution to the system, we need to optimize the trial function such that the error with respect to our governing equation is minimized.

In Finite Volume this is done using the subdomain method where the weighting function is described by equation 2.8 where $W_p(\mathbf{x})$ is our weighting function for the pth control volume, V_p is the pth control volume, and V is the volume of the whole system [14] [80]. When we apply the weighting function to the governing equation, with our trial function, and integrate over the whole simulation domain we get a series of residuals that can be minimized by optimizing the trial function $\phi'(\mathbf{x}, t)$. The equation for the residual corresponding to the pth control volume (R_p) is given by equation 2.10.

$$W_p(\mathbf{x}) = \begin{cases} 1 & \text{inside of } V_p \\ 0 & \text{outside of } V_p \end{cases} \tag{2.8}$$

$$R_p = \int_V W_p(\mathbf{x}) \left[\frac{\partial}{\partial t} \rho \phi' - \nabla \cdot (\Gamma \nabla \phi') - Su \right] dV \tag{2.9}$$

$$R_p = \int_{V_p} \left[\frac{\partial}{\partial t} \rho \phi' - \nabla \cdot (\Gamma \nabla \phi') - Su \right] dV \tag{2.10}$$

Before we proceed further let's discuss the meshing and spatial discretization scheme that will be employed. Cell centered meshing was used to split up the simulation domain into cells or control volumes. Under the cell centered scheme there is a co-location point in the center of each cell. Furthermore, each cell is contiguous with its neighbor cells such that they are adjacent, do not overlap, and each face is shared between neighbor cells (except for faces used in external boundaries) [42]. This is depicted in figure 2.7.

Also of importance is the placement of the co-location point p within the volume of the cell. Point p is located at the centroid of the cell such that equation 2.11 holds true. $\mathbf{x}$ is any vector that points from the origin to any point within the cell; while $\mathbf{x_p}$ is the vector that points from the origin to point p [42].

$$\int_{V_p} (\mathbf{x} - \mathbf{x_p}) \, dV = 0 \tag{2.11}$$

We can define a local trial function ($\phi'_p(\mathbf{x})$), centered about point p as defined in equation 2.12. ϕ_p is the value of the field ϕ point p; while $(\nabla \phi)_p$ is the gradient of the field
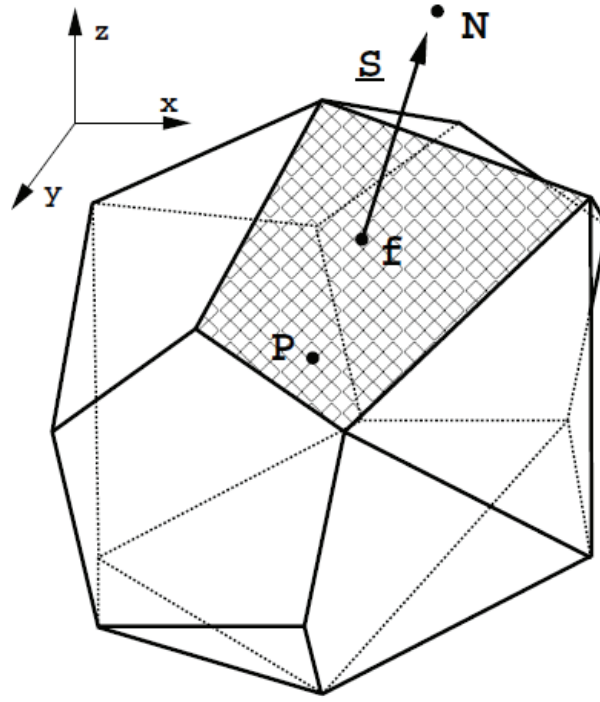
Figure 2.7: Cell Centered Mesh Element Schematic [42]

evaluated at point p. This trial function is linear in space, and can be used to achieve second-order accuracy in space where truncation error scales with $|(\mathbf{x} - \mathbf{x_p})|^2$ [42].

$$\phi_p'(\mathbf{x}) = \phi_p + (\mathbf{x} - \mathbf{x_p}) \cdot (\nabla\phi)_p \qquad (2.12)$$

2.4.2 Spatial Discretization

First let us consider the Laplacian component of our system. Based on the residual function described in equation 2.10, the spatial component in our system is categorized by the Laplacian term. The Finite Volume Method takes advantage of Gauss' Theorem in order to discretize the spatial derivative. Let us consider how we would apply Gauss' Theorem on an arbitrary vector field $\mathbf{a}$ as shown in equation 2.13 [42].

$$\int_{V_p} (\nabla \cdot \mathbf{a})\, dV = \oint_{\partial V_p} dS \cdot \mathbf{a} \qquad (2.13)$$

20

Based on our meshing, the cell (control volume) is bounded by a discrete set of flat faces f. As a result, the integral can be split up over each discrete face as shown in equation 2.14 [42].

$$\int_{V_p} (\nabla \cdot \mathbf{a})\, dV = \sum_f \int_f dS \cdot \mathbf{a} \tag{2.14}$$

If we assume that we have a linear variation in $\mathbf{a}$ similar to our assumption of linear variation in ϕ_p' (described in equation 2.12), we can approximate the surface integral in equation 2.14. Equation 2.15 describes how this is done, where $\mathbf{x_f}$ is the centroid of face f. Correspondingly, $\mathbf{a_f}$ and $(\nabla \mathbf{a})_f$ are the value of $\mathbf{a}$ and gradient of $\mathbf{a}$ evaluated at $\mathbf{x_f}$ [42].

$$\int_f dS \cdot \mathbf{a} = \left(\int_f dS \right) \cdot \mathbf{a_f} + \left[\int_f dS(\mathbf{x} - \mathbf{x_f}) \right] : (\nabla \mathbf{a})_f = \mathbf{S} \cdot \mathbf{a_f} \tag{2.15}$$

Finally, the divergence of $\mathbf{a}$ can be written as shown in equation 2.16 where $\mathbf{S_f}$ is the surface normal vector for face f [42].

$$\int_{V_p} (\nabla \cdot \mathbf{a})\, dV = \sum_f \mathbf{S_f} \cdot \mathbf{a_f} \tag{2.16}$$

Using the exact same procedure we can discretize the Laplacian term in the residual equation for control volume p (equation 2.10) as shown in equation 2.17 [42] [62].

$$\int_{V_p} (\nabla \cdot (\Gamma \nabla \phi'))\, dV = \sum_f \Gamma \mathbf{S_f} \cdot (\nabla \phi)_f \tag{2.17}$$

Since the trial function varies linearly, the gradient term can be approximated by taking the secant between the centroid of the current control volume (cell p) and that of a particular neighboring cell (cell n). For orthogonal meshes (where $\mathbf{S}$ and $\mathbf{d}$ are parallel), the gradient can be determined using equation 2.18 where $\mathbf{d}$ is the vector that points from the centroid of cell p to the center of cell n as shown in figure 2.8. For non-orthogonal meshes, OpenFOAM uses an additional term that interpolates gradients between neighboring cells [42] [62].

$$\mathbf{S} \cdot \nabla \phi = \frac{|\mathbf{S}|}{|\mathbf{d}|} (\phi_n - \phi_p) \tag{2.18}$$
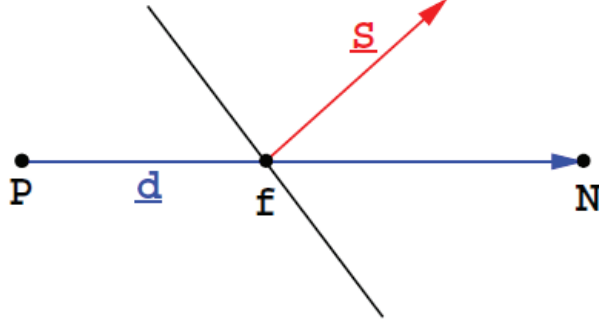
Figure 2.8: Cell Boundary Schematic

2.4.3 Time Stepping

Time stepping is achieved by discretizing the accumulation term in the residual function (equation 2.10). However, first we need to take care of the spatial dependence in the accumulation term. This is achieved by taking advantage of the fact that linear operators can be interchanged. In this formulation, we will isolate and solve for the spatial component of the accumulation term first, as shown in equation 2.19 [42] [62]. It should be noted that the mesh is consist throughout the entire simulation.

$$\int_{V_p} \left(\frac{\partial}{\partial t} \rho \phi' \right) dV = \frac{\partial}{\partial t} \int_{V_p} \rho \phi' dV \tag{2.19}$$

We can solve for the spatial component using the trial function we defined previously (equation 2.12). This is shown in 2.20 [42] [62].

$$\int_{V_p} \rho \phi' dV = \rho \int_{V_p} [\phi_p + (\mathbf{x} - \mathbf{x_p}) \cdot (\nabla \phi)_p] \, dV = \rho \phi_p V_p \tag{2.20}$$

In order to preserve the second order accuracy (we used a second-order accurate time stepping method maintain the accuracy of transient date), a second order backward differencing scheme was used to approximate the first temporal derivative of some arbitrary scalar field b. First lets start by taking the Taylor Series of b as a function of time and centered around time t. One such Taylor Series was used to find b at the previous time step $(b^{t-\Delta t})$ as shown in equation 2.21. Similarly, we can find determine the value of the b

at two time steps prior ($b^{t-2\Delta t}$) as shown in equation 2.22 [42]. Note, both the first ($\frac{\partial b}{\partial t}_t$) and second ($\frac{\partial^2 b}{\partial t^2}_t$) derivatives of b are both evaluated at the current timestep t.

$$b^{t-\Delta t} = b^t - \Delta t \frac{\partial b}{\partial t}_t + \frac{1}{2}\Delta t^2 \frac{\partial^2 b}{\partial t^2}_t + O(\Delta t^3) \tag{2.21}$$

$$b^{t-2\Delta t} = b^t - 2\Delta t \frac{\partial b}{\partial t}_t + 2\Delta t^2 \frac{\partial^2 b}{\partial t^2}_t + O(\Delta t^3) \tag{2.22}$$

By combining these two Taylor series we can cancel out the second time derivative term and find an approximation that is accurate to $O(\Delta t^3)$ as shown in equation 2.23 [42] [62].

$$\frac{\partial b}{\partial t}_t = \frac{3b^t - 4b^{t-\Delta t} + b^{t-2\Delta t}}{2\Delta t} \tag{2.23}$$

Finally, be combining equations 2.19, 2.20, and 2.23 we can define the discretized accumulation term as shown in equation 2.24 [42] [62].

$$\int_{V_p} \left(\frac{\partial}{\partial t}\rho\phi'\right)_t dV = \frac{3(\rho\phi_p V_p)^t - 4(\rho\phi_p V_p)^{t-\Delta t} + (\rho\phi_p V_p)^{t-2\Delta t}}{2\Delta t} \tag{2.24}$$

One should note, that this time stepping method is unconditionally stable [42].

2.4.4 Explicit Source Term

Lastly, the explicit source term in the residual function (equation 2.10) can be defined as shown in equation 2.25 [42] [62].

$$\int_{V_p} Su \, dV = Su V_p \tag{2.25}$$

Chapter 3

Simulation Method and Conditions

The following section will describe how our model was constructed which includes a description of the governing equations and the assumptions we made. Furthermore, we will identify the various boundary conditions that we used in our models and justify the use of each. Figure 3.1 depicts a schematic of an examplary microfluidic system. Also included are the relevant material properties for every component in our simulations.

Prior to simulating our system we developed an exploratory analytical model to determine general behaviour of the device. This analytical model consisted of simplified system which loosely resembles the actual design. For simplicity we limited ourselves to a one dimensional system at steady state.

Finally, this chapter will also describe how we implemented our simulation in `openFOAM`. This includes a description of the configuration files that were used as well as the steps required to run a simulation.

3.1 Assumptions and Model Description

The simulations presented herein describe the transient 3D temperature profiles of various designs of stationary single chamber PCR reactors. Each reactor is composed of several thin film layers that are patterned to include fluid regions. During operation, the fluid within the device is stagnant. Using dimensional analysis ($Ra << 1$), we found that we can neglect the effects of natural convection in internal fluid regions since these layers are too thin ($\approx 100\mu m$) and because the expected vertical temperature gradient ($\approx 5°C$) is too
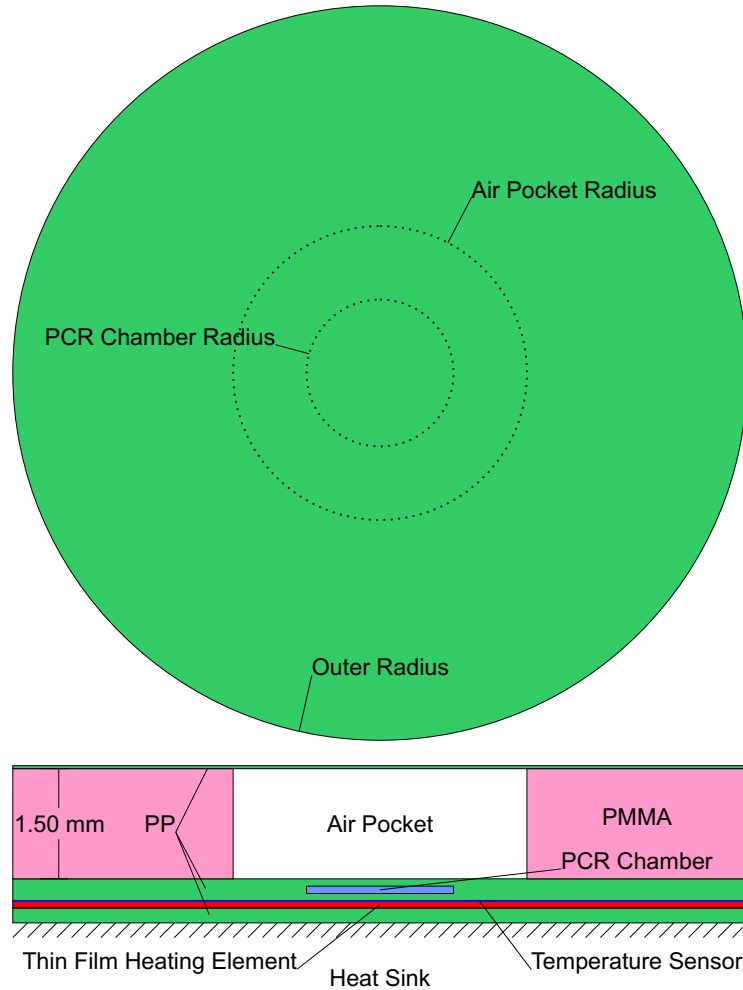
Figure 3.1: A schematic of of an example microfluidic PCR device: (a) top view and (b) cross section.

small to induce convective flow. Finally, we also neglected any heat of reaction since the heat supplied by the heating element was several orders greater than the heat of reaction.

`OpenFOAM` models the heat equation in terms of enthalpy as shown in 3.1. As mentioned before, convection terms have been omitted. Since we have omitted fluid flow, and we are neglecting the thermal expansion in this model, we can relate the enthalpy, shown in equation 3.1, to temperature using equation 3.2. Furthermore, we have included a bulk

generation term that is intended to simulate heating elements presenting in a particular design.

$$\rho_i \frac{\partial H_i}{\partial t} = \nabla^2(\alpha_i H_i) + q_i \tag{3.1}$$

$$dH_i = c_{Pi}dT \tag{3.2}$$

In equation 3.1 i is an index for each region present in the simulated system. Equation 3.1 describes conservation of energy for the ith region in terms of enthalpy of the ith region (H_i). T_i represents the three dimensional temperature profile of the ith region. ρ_i and c_{Pi} are the mass density and specific heat capacity of the ith region. Furthermore, α_i is defined as κ_i/c_{Pi}. Similarly, κ_i is the thermal conductivity of the ith region. Finally, q_i represents the input power density supplied to the system via Joule Heating by an external power source.

In order to account for various material properties present in a given design we conducted multi-region simulations. Each region was coupled to adjoining region via two internal boundary conditions. First and foremost, we are assuming that all regions are well coupled. As a result the temperature at an interface is coupled together in adjacent regions as shown in equation 3.3. The second condition that couples adjoining regions is described by equation 3.4. This condition states that heat flux must be conserved across internal boundaries.

$$T_i(\mathbf{n} = n_{ij}) = T_j(\mathbf{n} = n_{ij}) \tag{3.3}$$

$$\kappa_i \frac{\partial T_i}{\partial \mathbf{n}}(\mathbf{n} = n_{ij}) = \kappa_j \frac{\partial T_j}{\partial \mathbf{n}}(\mathbf{n} = n_{ij}) \tag{3.4}$$

For equations 3.3 and 3.4 we have two regions, region i and region j. The interface that separates these regions is denoted by n_{ij}. Correspondingly, $\mathbf{n}$ describes a vector normal to the n_{ij} interface which points from the ith region to the jth region. Finally, κ_i and κ_j represent the thermal conductivity of the ith and j^{th} regions.

In order to heat the reactor, our systems feature thin film heating elements that are composed of a snaking wire encased in a plastic matrix. When current is passed through these wires heat is produced through Joule heating. These systems are designed to provide uniform heating across the surface of the device. In order to achieve this, the wire is packed

tightly so that the separation between adjacent wire segments is small compared between the wire and surface of the thin film heating element. As such, it can be treated as a uniform bulk heating term. In order to simplify our model, we made the approximation of uniform heat generation (q_i) throughout the bulk of the heating elements, as shown in 3.1, where the heat generated through Joule Heating is averaged over the whole volume of the thin film heating element. q_i can be related to the electrical current running through the wire as shown in equation 3.5.

$$q_i = \frac{I_i^2 R_i}{V_i} \tag{3.5}$$

I_i is the electrical current running through the ith heating element. Similarly, R_i is the electrical resistance associated with the ith heating element. Lastly, V_i is the volume of the ith region.

The designs presented hereafter all feature a Heat Sink. The primary role of this heat sink is to improve the performance of any reactor design during cooling steps. We have assumed that we have an ideal heat sink for our simulations. This can be modeled using a Dirchlet boundary condition as described by equation 3.6.

$$T_i(\mathbf{n_{HS}} = n_{HS}) = T_{amb} \tag{3.6}$$

The ambient room temperature is denoted by T_{amb}. In our simulations the heat sink is always fixed to room temperature throughout the operation of the device. $\mathbf{n_{HS}}$ represents a vector normal to the heat sink boundary; which points out of the system. Similarly, n_{HS} represents the heat sink boundary interface.

Several designs are also exposed to the surroundings along at least one surface. The simulations featured in Chapter 5 consisted of the entire microfluidic chip, resulting in many surfaces exposed directly to air. In order to account for this we will model the air-plastic interface using a convective boundary condition as depicted in equation 3.7. Since the device is so small compared to the surrounding environment, we will assume that the ambient room temperature is unaffected by the operation of our PCR reactor. Similarly, we will consider the ambient room temperature to be fixed throughout operation. On a different note, the convective heat transfer coefficient (h) is a parameter determined by the flow rate of air above the surface of the device. For natural convection it can vary from $5W/mK$ to $25W/mK$. In our case our device will be shielded by external enclosure so we can expect this parameter to be close to the minimum. In our simulations we will assume that the convective heat transfer coefficient (h) is $5.6W/mk$ and does not vary throughout

the operation of the device. It should be noted, that the designs presented in the later chapters are largely insensitive to changes in the convective heat transfer coefficient. This is due to the placement of the heating element, heat sink, PCR chamber, and a sealed air pocket. The PCR chamber is nested between the heating element and the air pocket. This air pocket is used as insulation, where the thermal resistance of both the PCR chamber and convective boundary are negligible compared to the thermal resistance of the air pocket. Furthermore, the heating element is sits between the PCR chamber and the heat sink. As a result, most of the heat is directed into the heat sink.

$$-\kappa_i \frac{\partial T_i}{\partial \mathbf{n_C}}(\mathbf{n_C} = n_C) = h\left(T_i(\mathbf{n_C} = n_C) - T_{amb}\right) \tag{3.7}$$

As before κ_i is the thermal conductivity of the ith domain. h is the convective heat transfer coefficient of air. $\mathbf{n_C}$ is a normal vector that points outward along the convective boundary. Lastly, n_C represents the position of the convective boundary.

The designs presented in Chapter4 had cylindrical symmetry where the top and bottom boundary conditions are well known. Radially, there is no concrete boundary condition we can use. As a result we have to apply some assumptions to properly specify our system.

Firstly, we are simulating the PCR chamber in isolation. That is to say that there are no other features being represented (i.e. channels can be neglected) in our simulations. Consider the cross-sectional area of a typical channel to be about $100\mu m$ by $100\mu m$. The plastic surrounding such a channel can be $1.5mm$ thick; as a result, channels are a minor perturbation in the temperature of the surrounding plastic.

The second assumption we will make is that chip is "infinitely" large compared to the PCR chamber and surrounding features. A typical chip, fabricated using the same technique, will be approximately be $5cm$ by $5cm$. A PCR well is typically placed in the center of the chip and can have a radius of few millimetres.

By making these two assumptions, we can treat the chip to be infinitely large and featureless. Consider the temperature profile at some arbitrary point far away from the PCR chamber. Since there are no radial features, the temperature profile would be uniform in the radial direction. The designs presented in Chapter 4, all have a heating element adjacent to the heat sink. As a result, we can expect heat flow in the vertical direction to dominate (along the z-axis) as compared to the heat flow in the radial direction, where most of the heat loss experienced by the system is directed through the heat sink. Therefore, using Order-of-One scaling analysis we can define an outer radius around the PCR chamber where the temperature no longer varies radially. Mathematically this can be described by equation 3.8.

28

$$\frac{\partial T_i}{\partial \mathbf{r}}(\mathbf{r} = R) = 0 \tag{3.8}$$

$\mathbf{r}$ is a vector that points out from the center of the PCR chamber radially. R is an outer radius where we can consider the radial heat flow to be negligible.
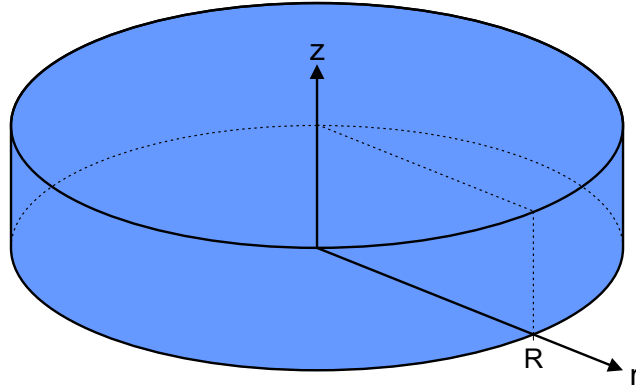
Figure 3.2: Single Region Radial Geometry

In order to find an acceptable outer radius lets consider the simplest case where we have a single radial region as shown in figure 3.2. Given the governing equation for this case, as shown in equation 3.9.

$$\rho c_P \frac{\partial T}{\partial t} = \kappa \frac{1}{r} \frac{\partial}{\partial r}\left(r \frac{\partial T}{\partial r}\right) + \kappa \frac{\partial^2 T}{\partial z^2} \tag{3.9}$$

Order-of-One scaling analysis was done to determine when the radial component of equation 3.9 can be neglected. It was found that the characteristic length of the radial direction (R_s) was equal to the characteristic length in the vertical direction (Z_s). Moreover we showed that the importance of the radial component of the heat equation scales with the square of the ratio of the characteristic lengths of the radial and vertical directions respectively $((R_s/Z_s)^2)$ as shown in equation 3.10. Note, t_s is the time scaling constant, and R_s and Z_s are the spatial scaling constants for the radial and vertical directions respectively.

Material	Mass Density $\rho(\text{kg/m}^3)$	Specific Heat Capacity $c_P(\text{J/kgK})$	Thermal Conductivity $k(\text{W/m}^2\text{K})$
Poly(propylene) (PP)	900	1500	0.2
Poly(methylmethacrylate) (PMMA)	1180	1500	0.2
Kapton (heating element)	1420	1090	0.12
Air	1.30	1000	0.024
Water (PCR chamber)	1000	4180	0.58
Copper	8790	385	401
Brass	8550	380	97

Table 3.1: Material Properties.

$$\frac{\rho c_P}{\kappa} \frac{Z_s^2}{t_s} \frac{\partial T}{\partial t} = \frac{R_s^2}{Z_s} \frac{1}{r} \frac{\partial}{\partial r}\left(r \frac{\partial T}{\partial r}\right) + \frac{\partial^2 T}{\partial z^2} \tag{3.10}$$

As a result, we used a cut-off radius ten times the total height of the simulated system. Under these conditions, it can be seen that at this cut-off radius (R) the temperature gradient in the r-direction will be negligible compared to that of the z-direction. Under these conditions we can use equation 3.8 for our radial boundaries.

3.1.1 Material Properties

Our designs featured multi-region devices composed of varying materials with varying thermal properties. The material properties of each material used are summarized in 3.1.

3.2 1D analytical Model

As a starting point in our investigation of PCR design we developed a steady state one-dimensional analytical model. This model was used to determine general performance characteristics of devices that would be later simulated. Using these models, we were able to relate the physical features of our device to its performance. We used this to develop our initial designs prior to evaluating them using numerical simulation. For example, these model was used to optimize the spacing between the heating element and the heat sink.

As a first order model we only looked at the temperature profile in the z-direction. Since, the systems being investigated here are all constructed of thin polymer layers to be

adhered to a heat sunk substrate; we can make the assumption in the limit of an "infinitely wide" design we can treat it as a one-dimensional system where the temperature varies in the z-direction only. As such, this one-dimensional approximation still contains multiple domains. For this reason, we solved for the steady state case. Due to the internal boundary conditions linking adjacent regions, orthogonality/Sturm-Liouville theory breaks down (Sturm-Liouville theory is a method used to determine the eigenvalues for an analytical solution to boundary value problems involving homogeneous second order linear ODEs).

In the configuration we looked at, a single heating element positioned below the PCR chamber. In order to maintain temperature uniformity throughout the PCR chamber, an insulating material must be placed above the chamber. This insulating layer restricts heat flow in the upward direction thus reducing thermal gradients within the chamber.

We looked at a simplified four layer system as depicted in figure 3.3. The bottom of the device is heat sunk to ambient room temperature. Domain 1 featured an insulation layer whose purpose is to insulate the heating element so that the power required the PCR chamber to target temperature could be tuned. Domain 2 is the heating element. Unlike the other regions in this design, it has a bulk heating term used to simulate Joule heating. Domain 3 is the PCR chamber, which was assumed to be composed entirely of water with no chamber walls for simplicity. Finally, Domain 4 is an insulation layer above the PCR chamber that is used to manage the heat flow travelling through the PCR chamber. The top of domain is exposed to air, as described above this will be treated as an external Robin boundary condition (3.7).

This configuration represents what is typically observed in microfluidic systems. It is a starting point from which optimizations can be made.

The governing equation for the present configuration are described in equations 3.11 through 3.11.

$$0 = \kappa_1 \frac{\partial^2 T_1}{\partial z^2} \tag{3.11}$$

$$0 = \kappa_2 \frac{\partial^2 T_2}{\partial z^2} + q_2 \tag{3.12}$$

$$0 = \kappa_3 \frac{\partial^2 T_3}{\partial z^2} \tag{3.13}$$

$$0 = \kappa_4 \frac{\partial^2 T_4}{\partial z^2} \tag{3.14}$$
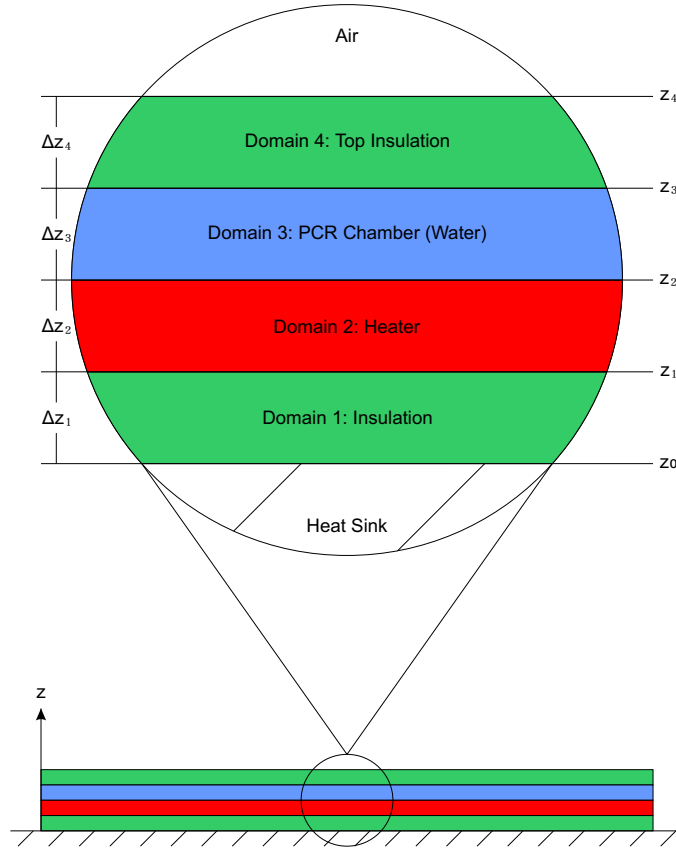
Figure 3.3: Simplified 1D Geometry

Instead of solving for the general case, let us instead parametrise the solution 3.13 based on a set of design metrics which are as follows. Namely the average temperature of the PCR chamber (domain 3) should be at our target temperature (T_{Targ}) (It is possible to do this exactly for this idealized system) and; the temperature variation within the chamber should meet some target variation (T_{Var}). More specifically we would specify that the average PCR chamber temperature is at our target temperature (T_{Targ}) as shown in 3.15 where ζ_3 is the thickness of the PCR chamber. Secondly, we can define a maximum allowable temperature variance within the PCR chamber (T_{Var}). In order to define the absolute temperature variation with the PCR chamber we will take the difference between

32

the maximum and minimum points as defined in 3.16. Finally, while not critical we should also seek to minimize the power consumption of the device.

$$T_{Targ} = \frac{1}{\zeta_3} \int_0^{\zeta_3} T_3(z)dz \tag{3.15}$$

$$T_{Var} = max(T_3) - min(T_3) \tag{3.16}$$

Based on the form of the governing equation for domain 3 (equation 3.13) we can see that the temperature can vary linearly across the thickness of the chamber as shown in equation 3.17. Note, in this formulation of the equation, the temperature profile of the PCR chamber is dependent on design specifications that are achieved by adjusting the geometry and input power of the device.

$$T_3(z) = -T_{Var}\frac{z}{\zeta_3} + \left(T_{Targ} + \frac{T_{Var}}{2}\right) \tag{3.17}$$

By solving for the temperature profiles of the other domains and applying our remaining boundary conditions for the other three domains we can generate a set of equations that relate our design specifications to the geometric parameters of our system. Firstly, by solving for domain 4, we can get a relationship that relates the thickness and material properties of this domain to the temperature variance experienced by the PCR chamber. This is described by equation 3.18 where ζ_i is the thickness of the ith domain, κ_i is the thermal conductivity of the ith domain, and h is the convective heat transfer coefficient of the air directly above domain 4.

$$\frac{T_{Var}}{T_{Targ} - T_{Amb}} = \frac{\kappa_3}{h\zeta_3} + \frac{\kappa_3\zeta_4}{\kappa_4\zeta_3} + \frac{1}{2} \tag{3.18}$$

Based on equation 3.18, we can see that the temperature variation within the PCR chamber is proportional to the desired target temperature. Therefore, when designing domain 4, we need to account for the worst case scenario encountered when denaturing the sample (i.e. $95°C$). Furthermore, we can see that the temperature variation within the PCR chamber is a function of both the thickness and thermal conductivity of domain 4, as well as the thermal properties of air directly above domain 4.

By solving for domains 1 and 2, we can find a relationship that shows how much power is required to achieve target temperature. The power density required to achieve the target

33

temperature is defined in equation 3.19, where q_2 is the power density applied in order to heat domain 2.

$$q_2 = \frac{\kappa_2}{\zeta_2} \frac{(T_{Targ} - T_{Amb}) + T_{Var}\left(\frac{1}{2} + \frac{\kappa_3 \zeta_1}{\kappa_1 \zeta_3} \frac{\kappa_3 \zeta_2}{\kappa_2 \zeta_3}\right)}{\frac{\zeta_2}{2} + \frac{\kappa_2}{\kappa_1}\zeta_1} \tag{3.19}$$

Based on this result, it can be observed that there is a inefficiency associated with heat flow leakage into the PCR chamber associated with T_{Var}. Furthermore, the denominator of equation 3.19 shows that the power required to achieve target temperature can be tuned by adjusting the thicknesses domains 1 and 2. As we increase the thickness of domain 1, less power is required to achieve target temperature since there is more insulation between the heating element and our heat sink. Similarly, a material with low thermal conductivity may be used in domain 1 in order to improve thermal insulation.

Overall, this configuration is relatively simple to manufacture but does not perform ideally. Since there is only one heating element, the temperature variation within the PCR chamber is fundamentally linked to the operating temperature of the system. Furthermore, variation in the PCR chamber, even in this idealized one dimensional simplification, is unavoidable. While temperature variation may be minimized by implementing better thermal insulation in domain 4, this also added more thermal mass to the system ultimately slowing down device operation. Finally, since there is a gradient in the PCR chamber, even at steady state, the power required to achieve target temperature will be greater than it would be had their been no power loss to the PCR chamber.

3.3 `OpenFOAM` Solver Modifications

`OpenFOAM` [78], an open-source computational fluid dynamics (CFD) library, was used. It provides a set of application-based solvers [27]. The standard solver for transient multi-region conjugate heat transfer simulations, `chtMultiRegionFoam`, was used which implements the finite-volume method [14] for spatial derivative approximation and the implicit Euler method for time-stepping [2] to solve the heat equation.

As a starting point for our simulations we used `chtMultiRegionFoam`, the standard multi-region heat transfer for both solid and fluid domains. This application solver already had built-in multi-region support, coupling between fluid and solid domains, and a large library of supported boundary conditions. In order for us to conduct our simulations we needed to make two modifications to the solver.

1. Firstly, we implemented a bulk generation term in the governing equation of each solid region. This was used as an explicit heat source which approximated the power density being fed to the heating elements in our system.

2. Secondly, when implementing feedback control in our simulations, it was necessary to further modify the solid region module. The solver was modified to store the proportional, integral and differential error as recorded by our simulated controller. While the controller itself was implemented using `swak4Foam` [35].

More importantly, we needed a solver that was general, in that it could simulate an arbitrary geometry with an arbitrary number of heating elements and sensors. As a result, we used a third-party software package called `Swak4Foam`. This package extends `OpenFOAM` allowing simple expressions to be evaluated at run time. This was particularly useful for implementing boundary conditions as well as for implementing the controller.

3.3.1 Bulk Generation Term

In order to incorporate the bulk heating term, we modified the governing equation for solid regions. The `chtMultiRegionFoam` solver natively solves the heat equation in terms of sensible enthalpy so that it can couple the effects of pressure and velocity for fluid regions. For a solid region the governing expression for the ith domain is given by equation 3.20 where ρ_i and α_i are constants related to the material properties of the ith domain.

$$\frac{d\rho_i H_i}{dt} - \nabla^2(\alpha T_i) = 0 \tag{3.20}$$

In order to implement a bulk heating term we modified the governing equation for a the ith as shown in equation 3.21 where q_i is a new parameter that represented a uniform power density applied across the ith domain. In order to implement this in `OpenFOAM` we modified the data structure for each solid region to include q_i.

$$\frac{d\rho_i H_i}{dt} - \nabla^2(\alpha T_i) - q_i = 0 \tag{3.21}$$

3.3.2 PID Controller Implementation

In our experimental system a PID controller was used to set the temperature of the PCR chamber using feed back loop [55]. The temperature of the PCR chamber was inferred

from a temperature sensor co-located near the PCR chamber itself. A PID controller takes this temperature and calculates the difference between the current temperature and the set point (err_P); it uses this information to regulate the input power of our heating element. In simulation we tried to emulate both the experimental geometry as well as the control system that was implemented, as a result we modified our numerical solver to include a generalized form of feedback control. The following section will outline, how a PID controller was implemented numerically in `OpenFOAM`.

In order to incorporate feedback control into our simulations, we need to first modify the application solver to support variables that store our error variables (i.e. proportional error, integral error, differential error). The native application does not support/keep track of variables not used in the solution to the governing equations for a given region.

Each error variable was treated as a property of the given region where the value at each time step was stored as a text file alongside the dependent variable. The advantage of this approach is that we can easily validate the output of the controller script.

In order to calculate the proportional error for the ith domain we subtracted the measured temperature from our current set point temperature as shown in equation 3.22. This operation is carried out at each time step.

$$err_P = T_{SetPoint} - T_{Measured} \tag{3.22}$$

One of the core features of `OpenFOAM` is a library of `FunctionObject`s that are executed during run time. Conventionally these objects are used to record simple operations to be used in post processing. For example, one could record the average temperature within a region using this method. However, with `Swak4Foam` this can be extended to affect defined properties relevant to the solver [35]. In particular we used the `manipulateField` library to modify existing domain properties. For example the following code segment is used to record the proportional error for the domain corresponding to a heating element within the system.

```
\label{lst_err}
h1.ramp1Err
{
    type                    manipulateField;
    functionObjectLibs      ("libswakFunctionObjects.so");
    region                  heater1;
    enabled                 true;
    verbose                 true;
```

36

```
        timeStart                    0;
        timeEnd                      100;
        outputControl                timeStep;
        outputInterval               1;
        variables                    "Tm{internalField 'solid2}=average(T);Ts=95;";
        fieldName                    err;
        expression                   "Ts–Tm";
        mask                         "true";
}
```

In order to approximate the differential and integral errors we need to discretize our simulation in time. For the differential error we can approximate the time derivative of the proportional error using a backward difference as shown in equation 3.23 where $err_{P,old}$ is the proportional error from the previous time step and Δt is the time step of the simulation. In this case it is important to note that measured temperature is defined by the user using this `FunctionObject` library and is related to the temperature in any domain present within simulated system.

$$err_D = \frac{derr_P}{dt} \simeq \frac{err_P - err_{P,old}}{\Delta t} \tag{3.23}$$

Similarly an integral error may be computed by approximating as shown in equation 3.24. Alternatively we can compute the integral error (err_I) recursively as shown in equation 3.25 where $err_{I,old}$ is the integral error from the previous time step.

$$err_I = \int_0^t err_P dt \simeq \sum_{t_0}^{N} (err_P \times \Delta t) \tag{3.24}$$

$$err_I \simeq err_{I,old} + (err_P \times \Delta t) \tag{3.25}$$

It should also be noted that the value of the integral error is dependent on when we start tabulating it. In our simulations we consider multiple temperature ramps with varying set point temperatures. As a result, the integral error is reset at the start of each ramping stage.

Using these error measurements we can set the power applied on the system using a simulated PID controller. Equation 3.26 describes the how the power density is set for the heating element in the $i^t h$ region using a PID controller where k_P, K_I and k_D are empirically derived constants.

$$q_{i,new} = (k_P \times err_P) + (k_I \times err_I) + (k_D \times err_D) \tag{3.26}$$

It should be noted that the simulated controller relies on explicit time stepping with constant time steps. As a result the error measurements at the current time step are used to update the power density for the next time step. As the time step gets larger there is a lag in the response of the controller. Furthermore, with larger time steps it is possible to get fluctuations and overshoots due to this lag. We limited our time step in order to prevent these errors.

3.4   Simulation Configuration

There are three main components in setting up a configuration directory for an `openFOAM` simulation, each of these elements is specified by its own folder. They are as follows:

1. "0": The `OpenFOAM` directory that typically contains the initial conditions. However, since we are implementing multi-region simulations, the 0 folder is used to holder dummy files for each variable in the simulation solver.

2. `constant`: This folder contains geometric information about the system as well as the material properties of each simulated regions.

3. `system`: This folder contains specifications for the simulation solver (i.e. which numerical schemes will be implemented) and error tolerances on the solver. Additionally the `system` folder houses the `controldict` which specifies the the runtime, time-stepping and control parameters of the simulation.

Additionally, there are two files housed within the main folder itself. The first is the `*.setSet` file which is used in constructing the simulation mesh. Finally, there is the `Preprocess` file which contains a sequential set of commands that initiate the simulation.

3.4.1   Initial/Boundary Conditions

Typically the initial conditions for a simulation would be housed in the 0 directory. However, in our case this folder holds a set of dummy files for each variable used in the simulation.

The `chtMultiRegionFoam` solver is the native `OpenFOAM` solver for transient heat transfer analysis with both fluid and solid regions. As such it can solve for fluid flow as well as heat transfer. Some of the dummy files housed in the `0` directory are related to fluid flow, they include: *epsilon*, p, p_{rgh}, and U. These were unused in our simulations. The `T` file stores the temperature profile within any given domain. In order to model a bulk generation term we modified the solver to add a new variable `expSrc`, which represents the bulk power density being pumped into a particular region (`expSrc` is equivalent to q_i in equation 3.1). Finally, the files marked `err*` are used to measure the proportional, derivative and integral errors during runtime and are specified by/related to the PID control system.

In order to actually, set the initial conditions of the simulation, the `changeDictionary` utility is used. As a part of its multi-region functionality, the `changeDictionary` utility allows users to specify the initial system conditions and external boundary conditions in a general way and allow for the system to assign them to the region(s) at run-time. This is particularly useful when working on simulations with many regions. Additionally, this utility has the added functionality in that it will automatically assign internal boundary conditions.

The `changeDictionary` utility is controlled by a `controlDictionaryDict` file contained within the `system` folder of each region. As such the initial conditions for each region may be tailored to each domain.

3.4.2   Meshing

At runtime, the mesh for the simulation is generated from a `blockMeshDict` file housed in `/constant/polyMesh`. It uses `openFOAM`'s built-in `blockMesh` utility to generate a single domain simulation geometry based on a simple set of commands.

Next this single domain is sliced into multiple regions as defined in the `*.setSet` file. This is done using `openFOAM` built-in utilities `setSet` and `splitMeshRegions`.

In the `constant` directory there is a folder that houses all of the geometrical data for each individual region. Prior to initialization, the only thing present in these folders are the material properties of each region. Since we are solving the heat equation for solid regions only, we only require `thermophysicalProperties` files which contain the mass density, thermal conductivity and specific heat capacity of each region.

Finally, there is a file within the `constant` directory called `regionProperties` which lets `openFOAM` know which regions are to be simulated and whether they are to be treated as solid regions of fluid ones.

39

3.4.3   Simulation Parameters

The `system` directory houses four important configuration files within each region directory. As discussed above, the `changeDictionaryDict` is used to set the initial and boundary conditions for the region. `fvSchemes` and `fvsolution` specify which numerical schemes will be used and what the tolerances of the solution are. `decomposeParDict` is a configuration file which is used to divide the simulation geometry into several small problems so that it can be solved using multiple cores.

The most important file in the `system` directory is the `controlDict` file which specifies the runtime controls to be executed as the simulation is run. In particular it is used to set the start time, end time, and the time step to be used. In order to implement feedback control, we also used the `FunctionObject` capabilities of `Swak4Foam` as discussed above.

3.4.4   Initialization

In order to initialize the simulation directory the `Preprocess` file is used. `Preprocess` is a bash script that carries out the following commands:

1. BlockMesh: Generates the base mesh that will become the simulation geometry.

2. setSet and splitMeshRegion: Slices up the base mesh into multiple regions as specified in the `*.setSet` file.

3. Remove unnecessary variable files from each region directory in order to minimize the memory requirements of the simulation.

4. changeDictionary: Assigns the initial conditions and external boundary conditions for each region.

5. decomposePar: Splits up the simulation so that it can take advantage of parallel processing across multiple machines.

Chapter 4

Initial Simulation Study of a Sample Microfluidic PCR Reactor

This initial study was based on a candidate design provided by our experimental counterparts, for which we wanted to validate the physical features of their design. In order to do this, we simulated an open loop heating ramp so we could make qualitative inferences about the temperature field of the system. The initial design work for this system was achieved using the lumped capacitance model, which was used to determine the steady state characteristics of the system as well as to determine heating/cooling time constant of the system. Given their initial system (as shown in figure 4.1) we constructed a high-fidelity multi-region transient heat transfer model to evaluate their system. In this initial study we limited ourselves to simulating a single heating ramp without the help of feedback control. Using our model we predicted key system characteristics including the simulated time constants of the system. Through this analysis we discovered a fundamental flaw in the embedded temperature sensor in the system. Finally, using our model we redesigned their system to improve sensor performance.

4.1   System Configuration

In this work, simulation-based engineering is used to evaluate a candidate design of a PCR microfluidic device (Figure 4.1). A conjugate heat transfer solver implemented as part of the open-source `OpenFOAM` library [78] is used for transient three-dimensional simulation of the proposed design. Specific objectives include:
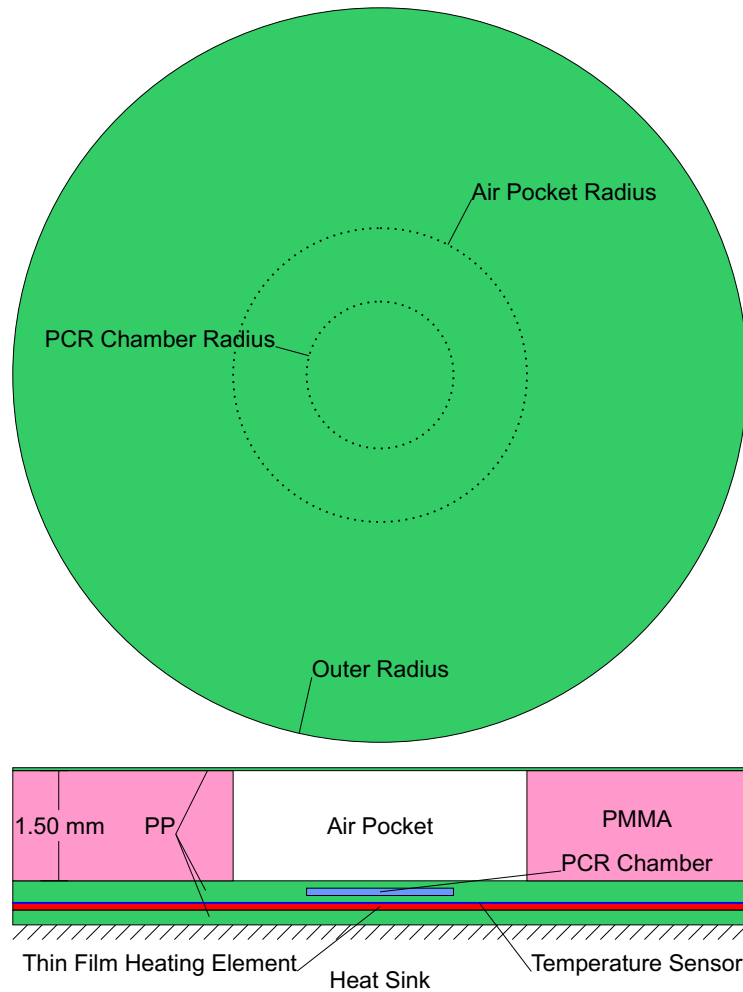
Figure 4.1: A schematic of the original microfluidic PCR device: (a) top view and (b) cross section.

1. Extension of the `OpenFOAM` conjugate heat transfer solver to include bulk heating in solid phases.

2. Evaluate a proposed PCR design, compatible with existing microfabrication techniques, for suitability such that PCR chamber temperature can be controlled to within ± 0.5K.

3. Relate the PCR chamber temperature from a quantity that is directly observable,

such as the heater temperature or the temperature measured by a sensor co-located with the heater. In the context of this problem it is of great interest to try and determine this quantity from the heater temperature (an average quantity).

4. Evaluate the dynamic time-scale response of the proposed design.

In this design, the thin film heating element doubled as a temperature sensor by monitoring the change in electrical resistance of the heating element as a function of temperature. It was found that the resistance of the heating element varies linearly with respect to the temperature of the heater over our temperature range of interest $(20°C - 100°C)$. As such we estimated the temperature recorded by the sensor (T_{Sen}) as the volume average temperature of the heating element domain as shown in equation 4.1, where V_{Sen} is the volume of the thin film heater.

$$T_{Sen} = \int_{V_{Sen}} T dV \tag{4.1}$$

4.2 Lumped Analysis

The most simple approach to indirect measurement of the PCR chamber temperature is through relating it to that of the measurable heater element temperature. Thus proximity of the PCR chamber to the heating element is key to reducing the discrepancy between the measured temperature and the actual temperature of the PCR chamber. Guided by this, a thin film design was developed with the maximum distance between the heating element and any point within the PCR chamber of 200μm.

Initially, lumped capacitance analysis [3, 43] was used to develop a prototype design. This method allows a rough approximation of the three-dimensional domain in the form of a linear circuit analogue. In this circuit, temperature differences between points in the system are analogous to a voltage differences, while heat flows are analogus to electrical currents. Each element in the system is modelled by a "resistor" and a "capacitor" where these are related to the solution of the heat equation in one-dimension [3].

$$R = \frac{d}{k\ A} \tag{4.2}$$

$$C = \rho c_p A d \tag{4.3}$$

where R and C are the thermal resistance and capacitance of an element in the system. Additionally, A is the area of a domain, d is the thickness of a domain.

By comparing different materials, a $100\mu m$ qPCR tape (AB1170, Fisher Sci) was selected for its PCR compatibility and thickness. Given volume of $2\mu L$ based upon a standard PCR protocol, the PCR chamber needed to have a radius of 2.5mm and a thickness of $100\mu m$. In order to implement a valve and pump structure, a 1.5mm PMMA structural layer is located on top of the thin film portion of the design. A recess is etched out of this film to reduce the thermal mass directly above the chamber.

In order to approximate the time constant of the system,

$$\tau = R_{Tot}C_{Tot} \tag{4.4}$$

the PP layer was "lumped" with the PCR chamber to determine a total thermal resistance (R_{Tot}). The total thermal capacitance (C_{Tot}) was calculated by summing the individual thermal capacitance values of each layer directly above the PCR Chamber. The thermal resistance (R_{Tot}) was found to be $R = 34.2K/W$, while the thermal capacitance of the system was determined to be $C = 0.013J/K$. As a result it was estimated that the time constant $\tau = 0.45s$ for heating the PCR chamber. Note that this time constant reflects the time required for heat to flow from the thin film heating elements into the PCR chamber, it does not take into account the time required for the thin film heaters to reach their target temperature.

4.3 Simulation-based Analysis

Preliminary tests using stationary simulations (steady-state) with different power densities (S) were performed to determine the appropriate value for a steady-state temperature of $95°C$. This temperature ramp represents the most extreme case of the PCR cycle. Thus simulations are limited to this case and a uniform power density of $0.41W/mm^3$ was used (6.4W for the entire device) which is representative of commercially available devices.

Simulation studies under heating were then performed for the proposed design. Analysis of the simulation results was guided by three target attributes (of the PCR chamber): temperature uniformity, response time, and heater temperature correlation. Subsequently, the time evolution of temperature in three areas in the domain was found through post-processing of the simulation data:

- *average PCR chamber temperature* – this will be the controlled quantity in the final device.

- *maximum deviation of PCR chamber temperature* – this quantity must be within tolerances under all operation conditions.

- *average heater element temperature* – this is the only directly measurable quantity given this problem definition.

From the temperature evolution within the PCR chamber and heater, characteristic response times of each of the domains may be computed indirectly through curve fitting to,

$$\frac{T(t) - T_{Amb}}{T_f - T_{Amb}} = 1 - \exp\left(-\frac{t}{\tau}\right) \tag{4.5}$$

where $T(t \to \infty) = T_f$ and τ is the characteristic response time.

The evolution of the temperature points throughout the simulation is shown in Figure 4.2. Significant variation within the PCR chamber with respect to the average temperature is predicted by the simulation, as shown in Figure 4.2. The maximum variation within the PCR chamber is over 2K, well above design specifications.

The characteristic response time of heating (τ) was found for both the average heater element temperature (1.45s) and PCR chamber temperature (2.54s) (please refer to Chapter 5 for more discussion about the characteristic response time). This difference is several times larger than the time constant predicted in the lumped capacitance model, which can be attributed to the lumped capacitance model neglecting heating of the thin film heater itself. There was also a large difference between the average temperatures within the heater and PCR chamber, which would complicate control of the device.

The cause of the large variation in the PCR chamber temperature was apparent from the simulation results. A major radial gradient in temperature at the central area of heater element/PMMA interface was observed, shown Figure 4.3. The simulation results show that this radial gradient has a significant effect on the PCR chamber temperature variation. Thus a modification to minimize this radial gradient would resolve this issue.

A design modification was made to counteract this issue was introduced which involved the addition of a 200μm layer of conductor (copper) directly above the heating element as shown in Figure 4.4. This highly conductive layer will only support a negligible gradient in temperature and will thus increase the radial uniformity at the PMMA interface. Simulations using this new design were performed under the same conditions as before, except for an increase in the bulk heating (applied power) in order to achieve the same target temperature. In order to reach a temperature of 95 °C a constant power density of 0.47W/mm^3 was applied (7.3W for the whole device).

Figure 4.2: Plots of temperature versus time for the original PCR device: (a) temperature evolution at different points within the device; (b) evolution of the total variation of temperature within the PCR chamber (solid line) and the difference between the average temperature of the PCR chamber and the measured temperature (dotted line).

The evolution of the temperature points throughout the simulation is shown in Figure 4.5. The variation within the PCR chamber with respect to the average temperature was predicted to decrease substantially, as shown in Figure 4.5. The maximum variation within the PCR chamber is less than 0.5K, below design tolerances. This is a direct result of the radial gradient in temperature at the central area of heater element/PMMA interface was decreased significantly, shown Figure 4.3. The only drawback in comparison with the original design is an increase in power to heat the device to the same temperature.

Finally, we found characteristic response time of heating for both the average heater element temperature (2.71s) and PCR chamber temperature (3.36s) in the new design by fitting our data to equation 4.5. However, due to the extra distance between the
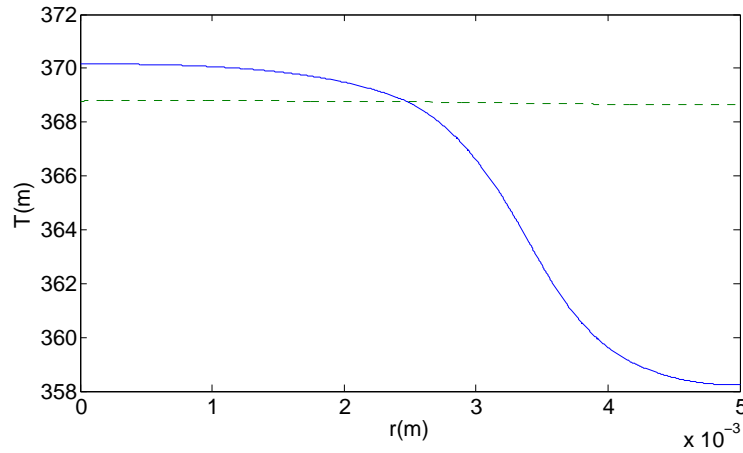
Figure 4.3: Radial temperature distribution of the top surface of the heating element from the original design (solid line) and the modified design (dotted line).
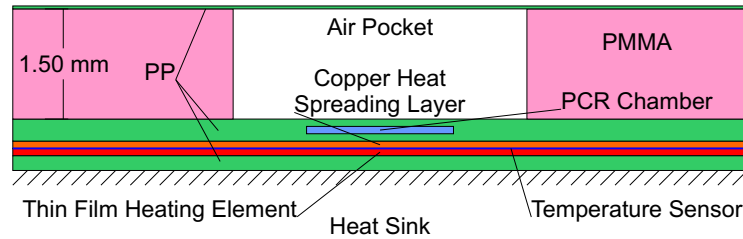
Figure 4.4: A schematic of the modified microfluidic PCR device (cross section).

heating element and the PCR chamber and because of the extra thermal mass added by the heat spreading layer, the time constants for the revised system were slow. Adding the heat spreading layer improved the correlation between the measured temperature and the temperature within the PCR chamber; after 10s the difference between these temperatures was only 1.47K.

4.4 Conclusions

Conjugate heater transfer analysis evaluation of a PCR chamber design was performed to determine its suitability with respect to response time and temperature uniformity. The dynamic time-scale of the proposed design was found to be approximately 2.54s for
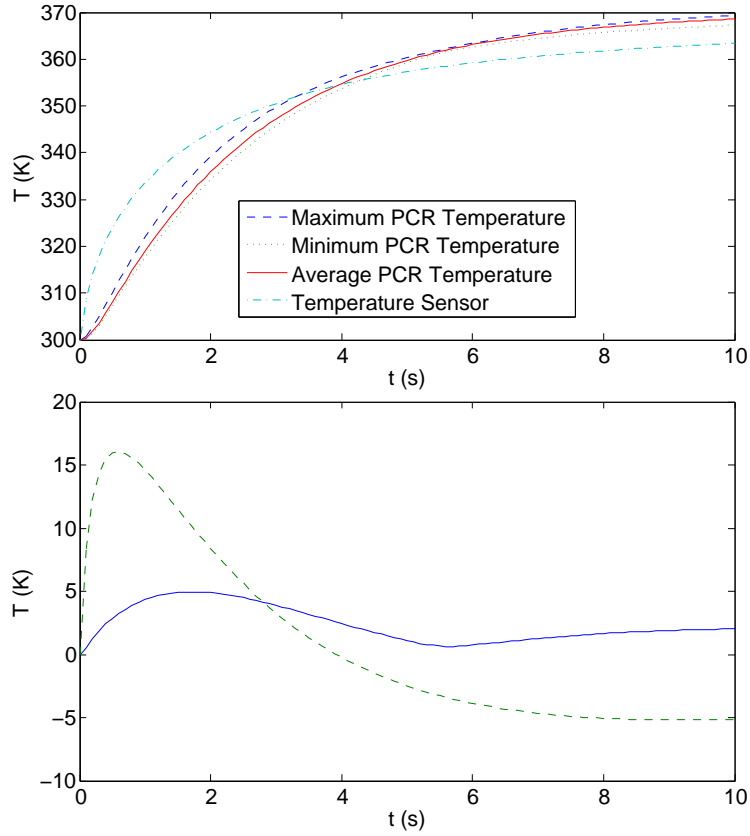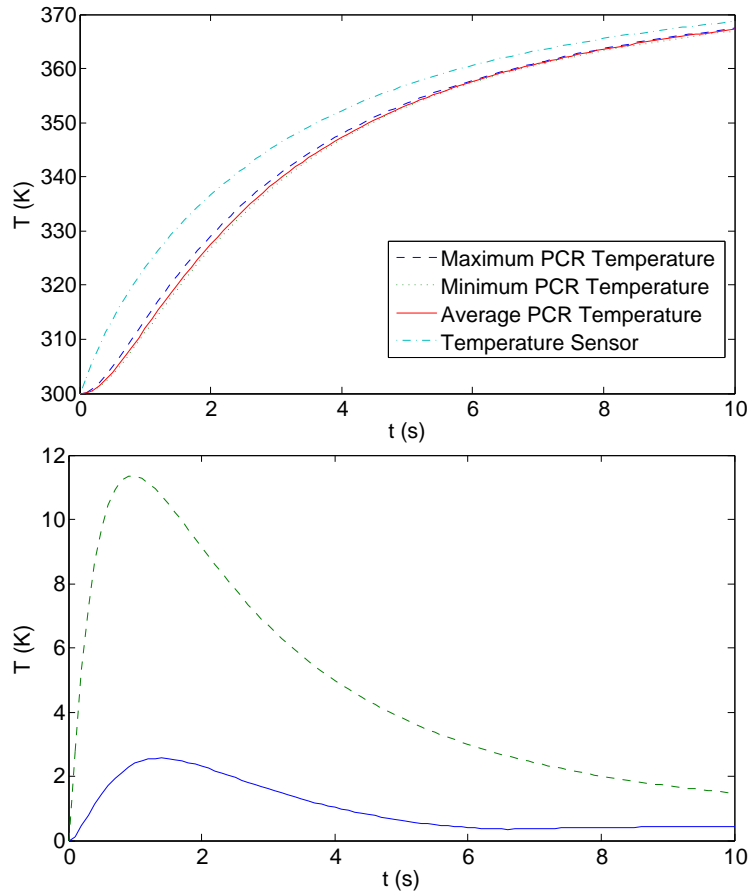
Figure 4.5: Plots of temperature versus time for the modified PCR device: (a) temperature evolution at different points within the device; (b) evolution of the total variation of temperature within the PCR chamber (solid line) and the difference between the average temperature of the PCR chamber and the measured temperature (dotted line).

experimentally accessible rate of heating. However, temperature uniformity within the PCR chamber in the proposed design was found to be greater than the acceptable limit of 1K.

A revised design was developed based upon the simulation results in which a conductive layer was added between the heating element and the PCR-chamber. The dynamic time-scale of the modified design was found to be approximately 3.36s for experimentally accessible rate of heating. Simulation of this design showed increased temperature uniformity of ±0.5K, below the acceptable tolerance without significant affect on the dynamic

48

response. However, the measured temperature of the heating element did not converge to the temperature in the PCR chamber within our allowed tolerance.

While we were able to make some significant observations with the simulations described in this chapter, we still need to integrate feedback control into our simulations to more accurately model the transient behaviour of experimental systems. Furthermore, In this chapter we looked at a single heating ramp. However, we also need to consider the cooling dynamics of PCR systems. The next chapter will address these concerns as well as compare our simulations against experimental analysis.

Chapter 5

Secondary Simulation Study of a Sample Microfluidic PCR Reactor with Feedback Control and Experimental Analysis

In this study we investigated a new PCR design based on the work that was previously done. Initially our experimental partners had tested there design and found that it was not successfully amplifying the target DNA sequence. Instead we were seeing the amplification of primer/dimers. We conducted a simulation study on this design that included feedback control as well as multiple PCR cycles simulated in sequence. We hoped to model the experimental system as closely as possible in order to identify the deficiency in the design. Through our simulation we were able to identify a transient discrepancy between the temperature of the measured temperature at our sensor and the PCR chamber. Using this information we modified the control scheme in order to allow the PCR chamber to catch up with the temperature sensor. When we re ran the same experiment with our new control scheme we found that system was able to successfully amplify the target sample DNA sequence.

The experimental work in this chapter was carried out by Gordon Hall, Tianchi Ma, and Madeline Couse.

5.1 Materials and Methods

5.1.1 System Design

The on-chip PCR reactor was designed in two parts: the PCR chip and heater system (Figure 5.1 and Figure 5.2). The chip was designed to be fabricated out of 1.5mm poly-methyl methacrylate (PMMA, Evonik) and polypropylene PCR tape (AB1170, Fisher) to allow for rapid-prototyping fabrication. It was fabricated using a $^1/_{16}$" endmill to create a 500μm deep and 1.6mm in radius well in the PMMA (Figure 5.2). The well is loaded with PCR reactants described in Section 5.1.3 and capped with a layer of PCR tape (Figure 5.2). Using this method, a batch of 6 PCR reactors can be built in less than 5 minutes.

The chip interfaces with a heater system built primarily out of PCR tape and centered on a commercially available heater (KHLV0502, 2" × 0.5", Omega) and thermocouple (Type K, Omega). An aluminum base is first machined with alignment pins to ensure alignment of the chip and the heater. Several layers of PCR tape are used as well defined thickness insulator layers (Figure 5.2) to separate the heater from the heat sink. Atop the PCR tape lies the heater as well which is nearly the same thickness as the PCR tape (Figure 5.2). A thin brass shim layer (Figure 5.2) was used to spread the heat from the heater; the heater has mm scale traces that would produce local temperature variations that need to be smoothed by a "spreader" layer. The thermocouple is also embedded in this brass layer to provide a more representative reading of the heater temperature. A 0.5" manifold was added to the system for future fluidic integrations. The manifold is spaced from the chamber to prevent it from interacting meaningfully with the PCR reactor. Figures 5.1 and 5.2 describe the entire system.

The temperature of the experimental PCR device was controlled using feedback control through embedded microcontroller and thermocouple measuring the heater layer temperature. Direct measurement of the PCR chamber temperature was not feasible due to its size and construction of the device.

In order to simulate the device we simplified the geometry as depicted in figure 5.3. Additionally, figure 5.3 depicts the boundary conditions which were used in our simulation.

5.1.2 Heat Transfer Analysis

Heat transfer analysis simulations were performed using the conjugate heat transfer solver in the `OpenFOAM` software library. `OpenFOAM` is an open-source simulation library which
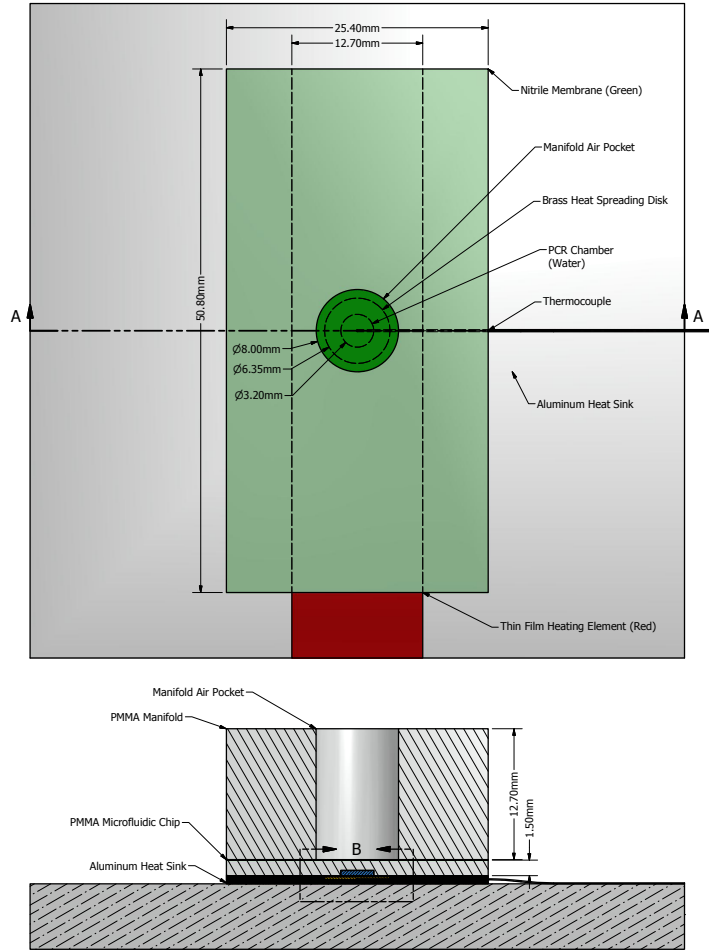
Figure 5.1: Schematic of prototype microfluidic PCR device design: (a) top-view; (b) cross-section A-A.

employs uses the Finite Volume Method (FVM) [78]. The conjugate heat transfer solver `chtMultiRegionFoam` provided by `OpenFOAM` was used to solve the conservation of energy equation within a simulation domain based on the experimental PCR design (see Supplementary Information). The simulation geometry, material parameters, and boundary conditions were specified to be commensurate with experimental conditions as feasible. Thus included full transient three-dimensional simulations with feedback control were performed with the following assumptions and simplifications:

1. *Symmetry:* two symmetry planes exist in the experimental design (Figure 5.1) which
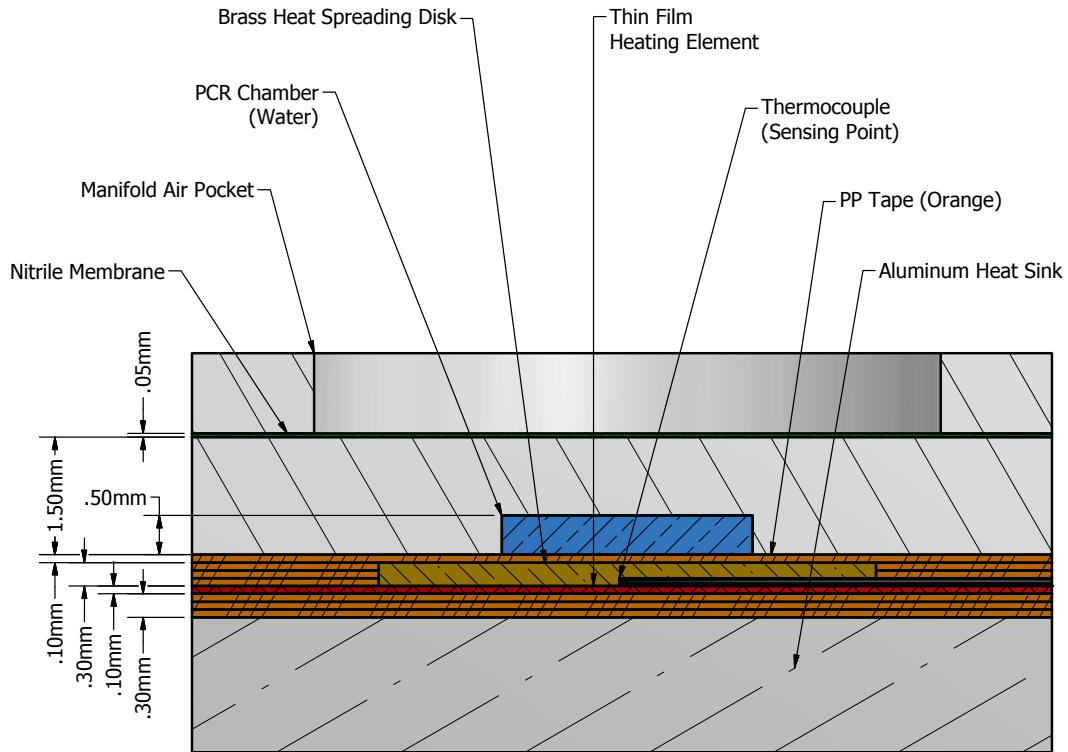
Figure 5.2: Schematic of prototype microfluidic PCR device design: Zoom in of the PCR Chamber Multilayer Structure.

were exploited in the simulations to reduce computational complexity.

2. *No flow:* fluid sub-domains were assumed to be at hydrostatic equilibrium and absent of flow.

3. *Convective heat transfer:* boundary conditions with the external environment above the PCR device were approximated using an empirical relationship for the heat flux with a convective heat transfer coefficient.

4. *Ideal heat sink:* boundary conditions with the external environment below the PCR device were assumed to be ideal, where the aluminum heat sink was assumed to be held at a constant ambient temperature.

5. *Uniform heating:* the thin film heating element was assumed to undergo spatially
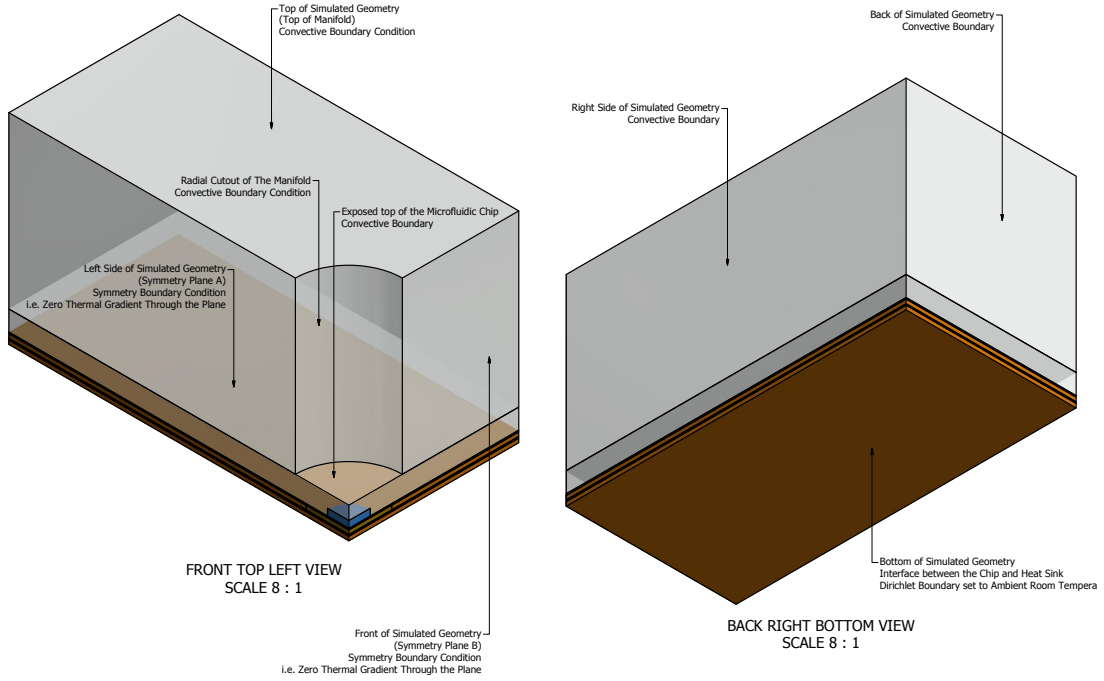
Figure 5.3: Schematic of Simulation Geometry with Boundary Conditions (a) front view; (b) back view.

uniform Joule heating in order to approximate the complex network of conducting wires encased in a plastic thin-film matrix. The Joule heating generated as a result of using the thermocouple was neglected since current being passed through the thermocouple is negligible compared to the current used to actuate heating ($\approx 1mA$ vs. $\approx 500mA$).

In the absence of flow for a homogeneous material, such as a sub-domain of the PCR device, the conservation of energy equation with respect to temperature is [5]:

$$\rho_i c_{P,i} \frac{\partial T_i}{\partial t} = k_i \nabla^2 T_i + S_{E,i} \tag{5.1}$$

where the index i refers to a homogeneous sub-domain, ρ_i density, $c_{P,i}$ is constant-pressure heat capacity, k_i is thermal conductivity, and $S_{E,i}$ is the bulk generation term.

Boundary conditions for each of the sub-domains, both solid and liquid regions, were assumed to be in close contact with each other so that temperature was continuous across

Variable	Description	Value
$T_i{}^*$	Temperature Profile of the ith region	
$\rho_i{}^*$	Mass Density of the ith region	
$c_{Pi}{}^*$	Specific Heat Capacity of the ith region	
$\kappa_i{}^*$	Thermal Conductivity of the ith region	
$S_{Ei}{}^*$	Input Power Density applied on the ith region	
$I_i{}^*$	Electrical Current applied on the ith region	
$R_i{}^*$	Electrical Resistance of the ith region	
$V_i{}^*$	Volume of the ith region	
$T_{amb}{}^*$	Ambient Room Temperature	$22°C$
h^*	Convective Heat transfer coefficient of free standing air	$5.6W/mK$

Table 5.1: Model Parameters.

each boundary. The surrounding environment above the PCR device was treated as an infinite heat reservoir,

$$\mathbf{n} \cdot (-k_i \nabla T_i) = h\,(T_i - T_{amb}) \tag{5.2}$$

where $\mathbf{n}$ is the unit normal (outward) of the boundary and h is a convective heater transfer coefficient. A value of $5.6W/m^2K$ was used to approximate free convection as in past work [38].

The relationship for S_{Ei} for the thin film heater is related to the power density of the heater. This is formulated in terms of input current:

$$S_{Ei} = \frac{I_i^2 R_i}{V_i} \tag{5.3}$$

where I_i is current, R_i is resistance, and V_i is voltage. Feedback control was implemented in simulations using the same parameters, including control loop timing, as the experimental device.

5.1.3 Biochemistry

Reagents

Genomic DNA was isolated from lymphocytes of individuals (obtained with informed consent) using a QIAamp DNA Blood Maxi Kit (QIAGEN, Canada), and dissolved in low

Tris-EDTA (TE) buffer (pH 8.0). PCR buffers, MgCl$_2$ and polymerase were from Invitrogen Canada. Primers were from Eurofins MWG Operon, USA. Bovine Serum Albumin (BSA) was from New England Biolabs. Agarose III^{TM} was from Amresco® Canada. 10X Tris-Borate (TB) buffer was prepared from Tris (tris (hydroxymethyl) aminomethane) (BioShop, Canada) and boric acid (EMD Chemicals, Canada), and was diluted to 1X and 0.1X with Milli-Q water.

Polymerase Chain Reaction Mixture

The polymerase chain reaction (PCR) was done both on-chip and using a conventional PCR machine. The primer pair used was designed to flank exon 2 of the HFE gene associated with hereditary haemochromatosis. The forward primer is unlabelled (5'-CAT ACC CTT GCT GTG GTT GTG ATT-3') and the reverse primer is labelled with Alexa Fluor 532 (5'-AminoC6 + Alexa 532 TCA GAG CAG GAC CTT GGT CTT TCC-3') for subsequent analysis. The resultant product is 234 bp. $20\mu L$ of PCR brew was made with the reagents in Table 5.2 and used for the PCR procedures.

Component	Volume	Final Concentration
Sterile Milli-Q H$_2$O	13.2	-
10x PCR buffer (with MgCl$_2$)	2	1X
MgCl$_2$ - 50mM	0.8	2mM
dNTPs- 10mM	0.4	200 μM
BSA- 10μg/mL	0.4	0.2 μg/μL
Forward Primer	0.4	400 nM
Reverse Primer	0.4	400 nM
Recombinant Taq- 5U/μL	0.8	0.2 U/μL
gDNA (15 ng/μL	1.6	1.2 ng/μL

Table 5.2: Components for PCR Brew

PCR Thermal Cycle Protocol

A PCR was performed using a conventional PCR machine using the $20\mu L$ brew described in Table 5.2. The thermal cycling protocol is listed in table 5.3. To perform the on-chip PCR first the chip described in Section 5.1.1 was cleaned with Milli-Q water. $4\mu L$ of the PCR brew in Table 5.2 was added to the PCR well and sealed with PCR tape. The chip was then pushed into contact with the brass spreading layer described in Section 5.1.1. The thermal

cycling protocol in Table 5.3 was input into the temperature controller. Comparing the conventional and on-chip PCR thermal cycling protocols, an extra 30 seconds was added to each step to account for a time constant difference between the heater layer that was being temperature controlled and the PCR reactor.

Step	Temperature	Time for Conventional (seconds)	Time for On-Chip (seconds)
1	95 ^{o}C	120	120
2	95 ^{o}C	10	40
3	65 ^{o}C	20	50
4	72 ^{o}C	20	50
5	GO TO 2 X 35	-	

Table 5.3: Thermal Cycling Protocol for Conventional and On-Chip PCR

Reaction Validation Procedure

Following the PCR reaction the resultant product was tested using microchip electrophoresis using a Micralyne Microfluidic Toolkit (μTK). Fluidic chips were fabricated through micro-milling as per previous work [37] with channel cross-sections of $250\mu m$ x $250\mu m$. The sieving matrix was 2.5% agarose in 1X TB buffer and the sample was diluted 1:10 with 0.1X TB. The separation was done at $100V/cm$.

5.2 Results and Discussion

In order to evaluate the system presented herein, we conducted a series of experimental tests that compared the on-chip device to a conventional PCR system. Effectiveness for the on-chip PCR device was determined through comparison with the conventional/commercial system. Performance of the on-chip control system could not be measured directly, thus simulation predictions for the system were used to predict the thermal response of the on-chip device. As such we conducted a series of simulations that mirrored the experimental system in both physical geometry as well as the control scheme.

5.2.1 Experimental Results

Figure 5.4a shows the temperature cycling result of the on-chip PCR. As can be seen, there is a 2 degree overshoot on the first melting step, but afterwards temperature rapidly reach

equilibrium for all 35 cycles. Thus, assuming that the PCR chamber to reaches our target temperature, one would expect to get successful amplification. To determine if successful amplification occurred the product of the on-chip PCR was compared to a conventional PCR machine product using microchip electrophoresis. The results of this comparison are shown in Figure 5.5

The blue trace in Figure 5.5 is the output of a conventional PCR – there are two clear peaks present. The first peak at approximately 79 seconds is due to unused primers leftover from the PCR. The second peak at 105 seconds is the product peak from the PCR. The absence of any other peaks would indicate a specific amplification occurred, and the fact that the peak heights are reasonably comparable indicates a reasonable conversion of primers to product. The green trace in Figure 5.5 is the output from the on-chip PCR. Three peaks are observed and are, from left to right, the primer, primer-dimer and amplified product. The fact that a discernible product peak is present indicates a very good conversion ratio and successful genetic amplification. However, the presence of the primer-dimer peak indicates a lack of uniformity in the system causing primer-dimers to non-specifically amplify. The slight time shift of the on-chip peaks to the right is within the limit of error of the microchip electrophoresis system used. This electropherogram suggests that the chamber temperature reached approximately the appropriate temperatures, but lacked in uniformity. Additionally, it was observed that the aluminum heat sink layer did deviate from ambient temperature during parts of the run.

5.2.2   Simulation Results

Thermal Time Constants

The initial simulation studies were performed in order to determine approximate thermal time constants for heating τ_h and cooling τ_c of the PCR device. These time constants are based upon an approximation of uniform conditions within the device and are useful for estimating the response time of the PCR device with respect to changes in set points. Given the uniform volume assumption, a macroscopic unsteady-state energy balance may be derived:

$$\rho c_p V \frac{d\bar{T}}{dt} = hA \left(\bar{T} - T_{amb} \right) + V S_E \tag{5.4}$$

where all quantities are uniform volume approximations: ρ density, c_p is heat capacity, $\bar{T}$ is temperature, V is device volume, and A is device surface area exposed to the environment. This equation can be solved under cooling ($S_e = 0$, where the initial condition of the system
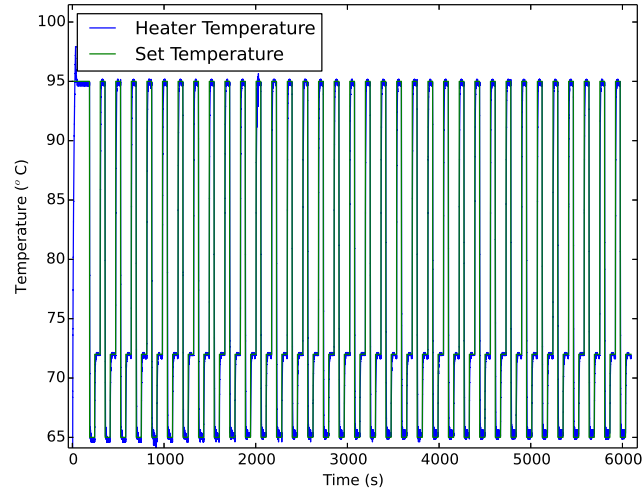
(a)
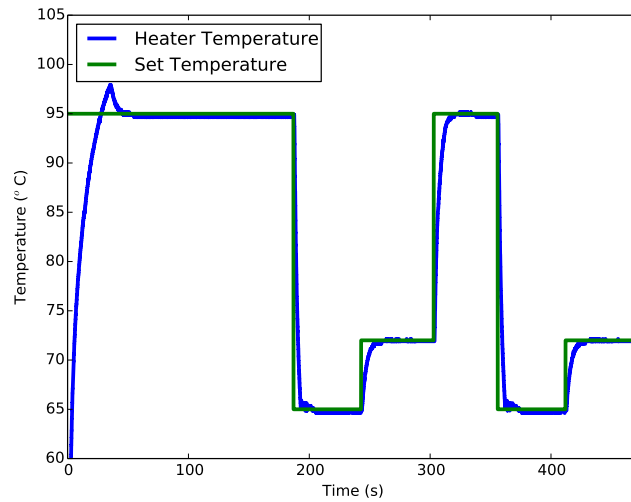
(b)

Figure 5.4: Experimental PCR temperature evolution for the PCR device for (above) 30 cycles and (below) the first two cycles (of 30).

is above ambient room temperature) conditions:

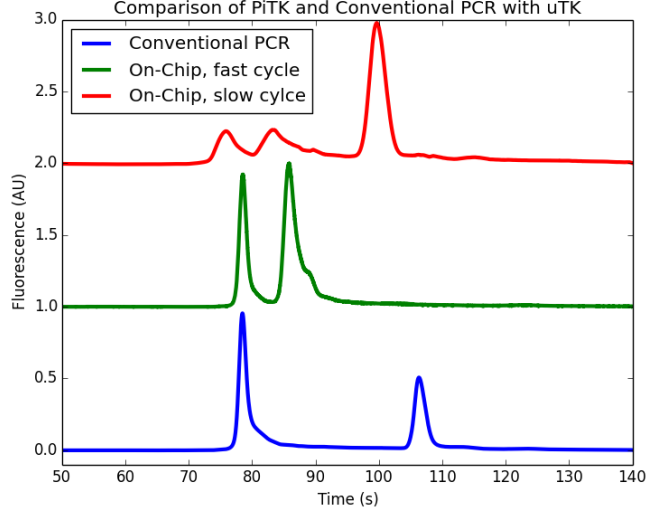$$T = T_0 \exp \frac{t}{\tau_c} \tag{5.5}$$

Figure 5.5: Electropherogram comparing PCR done using a conventional system and the on-chip system. The on-chip PCR shows successful amplification but the presence of the third peak indicates primer-dimer non-specific extensions

and heating ($S_e > 0$) conditions:

$$T = (T_0 - T_{eq}) \exp \frac{t}{\tau_h} + T_{eq} \tag{5.6}$$

where T_0 is the temperature of the device at $t = 0$, $T_{eq} = \frac{VS_e}{hA} + T_a$, $T \geq T_a$ is assumed. The approximate dynamic timescale for these processes are shown to be equal:

$$\tau = \tau_c = \tau_h = \frac{\rho c_p V}{hA} \tag{5.7}$$

for an ideal system.

Simulations of cooling and heating dynamics were performed in order to estimate τ using bulk heating values and initial conditions relevant to the experimental system. These simulations featured the same geometry, boundary conditions, and initial condition (everything is originally at ambient room temperature). However, in order to infer the time constants of the system we simulated the performance of the device under constant power. The thermal time constant τ was approximated from these simulations to be $15.19s$ for heating and $15.00s$ for cooling using the average PCR chamber temperature as the reference. This is quite different than the time constants found in the previous chapter. The

biggest reason for this discrepancy, is that the simulations in this chapter included a $1/2$"
manifold which acts as a heat reservoir in that it slows down the device. Figure 5.6 shows
simulations results for the heating and run along with the best-fit of equation 5.6. We
expect that the analytical solution to this system would have a series of exponential time
constants. As a result we can see that the curve of best fit deviates from the simulated
temperature at $\approx 75s$ due to the contribution of slower time constants. However, since
our regression curve fits the transient response of the system well, we can conclude that
the fastest time constant is dominant (the slower contributions can be neglected for short
ramping times) and can be approximated to first order accuracy using a single exponential.
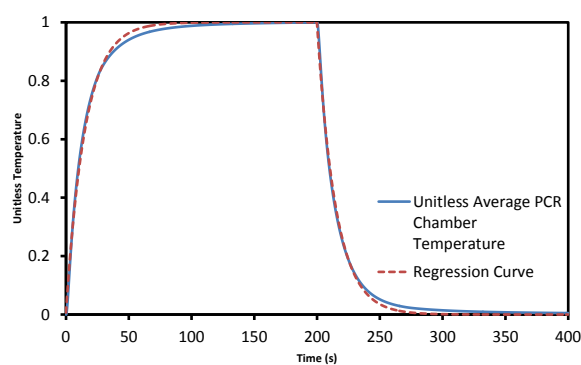
Figure 5.6: Simulation predictions for the average temperature of the PCR chamber with
curve fitting to predict the time constant of the PCR chamber

These simulation results predict that for both experimental PCR runs the dynamic
response time of the device was on the order of the time intervals allocated for each of the
PCR cycle steps. Thus it is possible that the characteristics of the device preclude the
possibility of the device control functioning optimally.

PCR Cycle Performance

In order to determined more descriptive predictions of the experimental PCR device per-
formance simulations were performed of the full PCR cycle. Simulation predictions of
the temperature evolution within the device is shown in Figure 5.7a including: average

PCR chamber temperature, sensor temperature, and set point temperature. Temperature evolution for the full 30 cycles (Figure 5.7a) and for the first two cycles (Figure 5.7b) are shown. The results for the first cycle differ from that for following cycles due to the initial condition of device (temperature profile) being uniform and at ambient temperature for the first cycle.
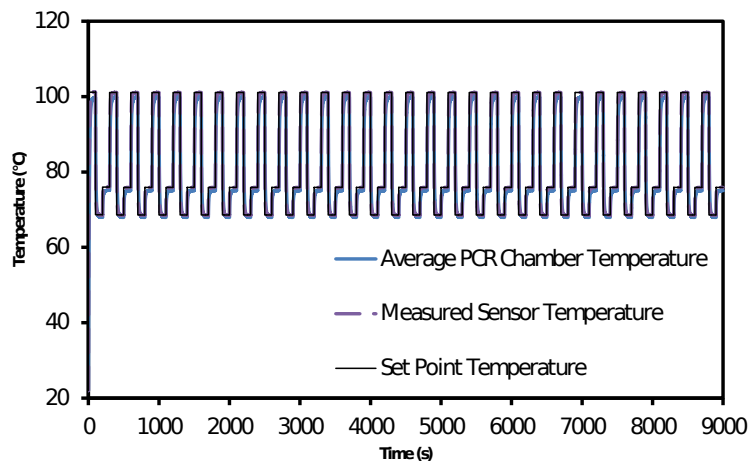
(a)
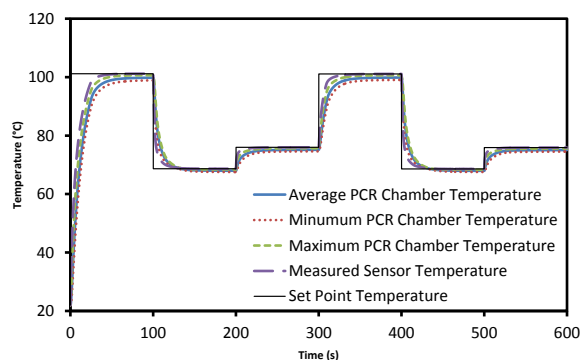
(b)

Figure 5.7: Simulated PCR temperature evolution for the PCR device for (above) 30 cycles and (below) the first two cycles (of 30).

Each temperature ramping step was simulated for $100s$, larger than that used for the ex-

62

Simulated Temperature ($°C$)	Denaturation	Annealing	Extension
Average PCR Chamber Temperature	99.80	67.99	75.16
Minimum PCR Chamber Temperature	98.90	67.54	74.61
Maximum PCR Chamber Temperature	100.65	68.41	75.67
Measured Temperature	101.16	68.66	75.99

Table 5.4: Key Temperatures within the Simulated System at Steady State (As closely as possible we tried work with the experimental control parameters, even so our simulated temperatures are sightly higher than expected. Clearly further adjustment would be needed to better determine the experimental control parameters.).

perimental system, to enable the controller to stabilize the temperature. This was done to predict the optimal performance of the experimental design while simultaneously enabling insights to be gained for conditions with shorter time intervals. As seen in Figure 5.8, the experimental design is able to achieve a PCR cycle, but even under optimal conditions the experimental design does not reach equilibrium. This simulation prediction is supported by experimental electropherogram results shown in Figure 5.5 indicating some degree of amplification occurs. Electropherogram results show significant primer and primer-dimer output which results which can now be attributed to non-optimal PCR cycle performance. Further analysis of the simulation results is shown in Figure 5.8 which show key temperature profiles for the first two PCR cycles. Simulations predict significant variation in both the temperature within the reaction chamber (Figure 5.8b) and deviation from the temperature sensor input (Figure 5.8c) which was used for control in both the experimental and simulation device. At the end of each of the extended cycle, the temperature variation within the reaction chamber ranges from $0.87 - 1.76°C$ which deviates from optimal PCR conditions. Table 5.4 summarizes the different important temperatures within the system at the end of each temperature ramping step.

Figure 5.9 shows the temperature profile within the device during each of the three PCR cycle stages: denaturation (heating), annealing (cooling), and extension (heating). The temperature variation in the PCR chamber can be decomposed into vertical (axial) and horizontal (radial) contributions. As shown in figure 5.9 the dominant thermal gradient lies along the vertical direction of the device, this would indicate that convective heat loss the dominant heat loss mechanism. The PCR device design is observed to admit higher gradients in the vertical direction than in the horizontal one due to both a lack of symmetry and power mismatch in the heating and cooling mechanisms. During heating cycles (denaturation, extension) the heating element is exposed to a much cooler/good conductor below (the heat sink) and a less cool/less effective conductor above (PCR cham-
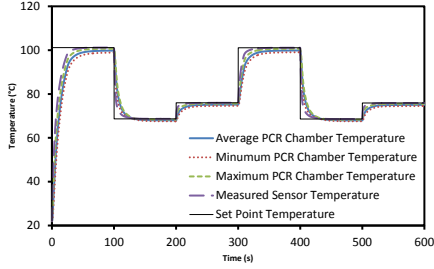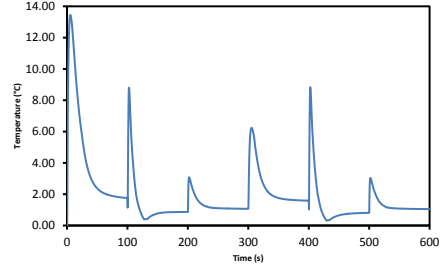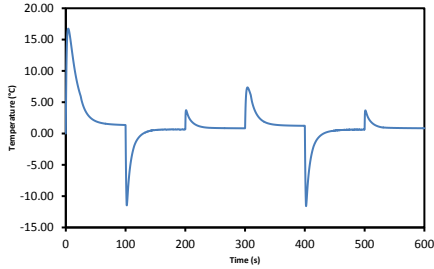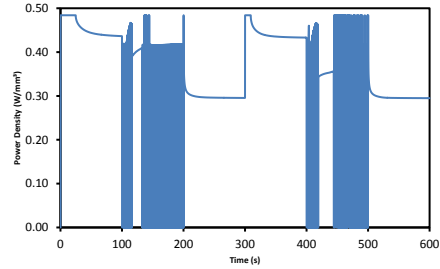
Figure 5.8: Simulation predictions for the evolution of the (a) sensor temperature and average/minimum/maximum reaction chamber temperature; (b) magnitude of the variation within the PCR chamber; (c) deviation of the sensor temperature from the average reaction chamber temperature; (d) device power consumption (Note that during cooling ramps the power input fluctuated wildly which resulted in the blotches observed in this figure).

ber and polymer layers). This requires relatively high power densities being applied to the heating element in order to overcome the significant heat flux through the conductive layer below. Subsequently, significant vertical temperature gradients are imposed on the PCR chamber and surrounding layers. While this scenario could be avoided through a symmetric design where the thermal diffusivity above and below that heater were matched, this would result in a significant increase in the cooling time of the device. Thus an engineering optimization problem exists due to the competition of heating and cooling characteristics with respect to the device design. This is further elucidated through analysis of the cool-

ing cycle (denaturation). The heater element side of the PCR chamber rapidly evolves towards ambient temperature due to the significant heat flux through the conductive layer below the heater. Conversely, the insulating properties of the polymer layers above the PCR chamber result in a much slower cooling process. The combined effect, again, are significant vertical temperature gradients in the PCR chamber during cooling.

The existence of significant vertical thermal variations also contributes to inefficiency of the control design, which uses a temperature sensor based on the average temperature in the heating element (Figure 5.1). Figure 5.8c shows the time evolution of the sensor error over time. It was determined that there was a non-linear relationship between the temperature of the PCR chamber and the temperature recorded by our sensor. This non-linear discrepancy between the PCR chamber and the sensor was largely transient, but at steady state we determined that there was an error proportional to the set point temperature. This error ranged from $0.67°C$ (during Annealing) to $1.36°C$ (during denaturation). This is well outside of our design specifications, the annealing stage is particularly sensitive to this sort of error, and it is expected that an annealing temperature cooler than what is intended would produce non-specific binding leading to amplification primer/dimers. This discrepancy is a function of proximity to the PCR chamber. Furthermore, the vertical thermal gradient mentioned previously also contributed to this problem.

Figure 5.8d describes the power usage of the simulated device through the course of our simulations. The power is controlled by the PID controller that we implemented where, the parameters of the system were experimentally tuned. These experimental parameters were converted to be compatible with our simulation package. In order to model the finite range of powers the experimental power supply could deliver, we implemented an upper and lower bound on the simulated power. Furthermore, at the start of each heating/cooling step the integral error was reset. In the case of cooling steps there was no integral gain, instead the power was shut off completely until the measured temperature was $0.5°C$ above the set point. Once this occurred, proportional and derivative gain were used along with a constant term to account for the integral term. In doing so it was found that the power input to the system was not stable during the cooling stages. However, the was no instability in the temperature of the PCR chamber itself. Since, rapid cooling during the annealing stage is important to PCR amplification, it is suggested that a PWM controller be implemented during the cooling stage instead.
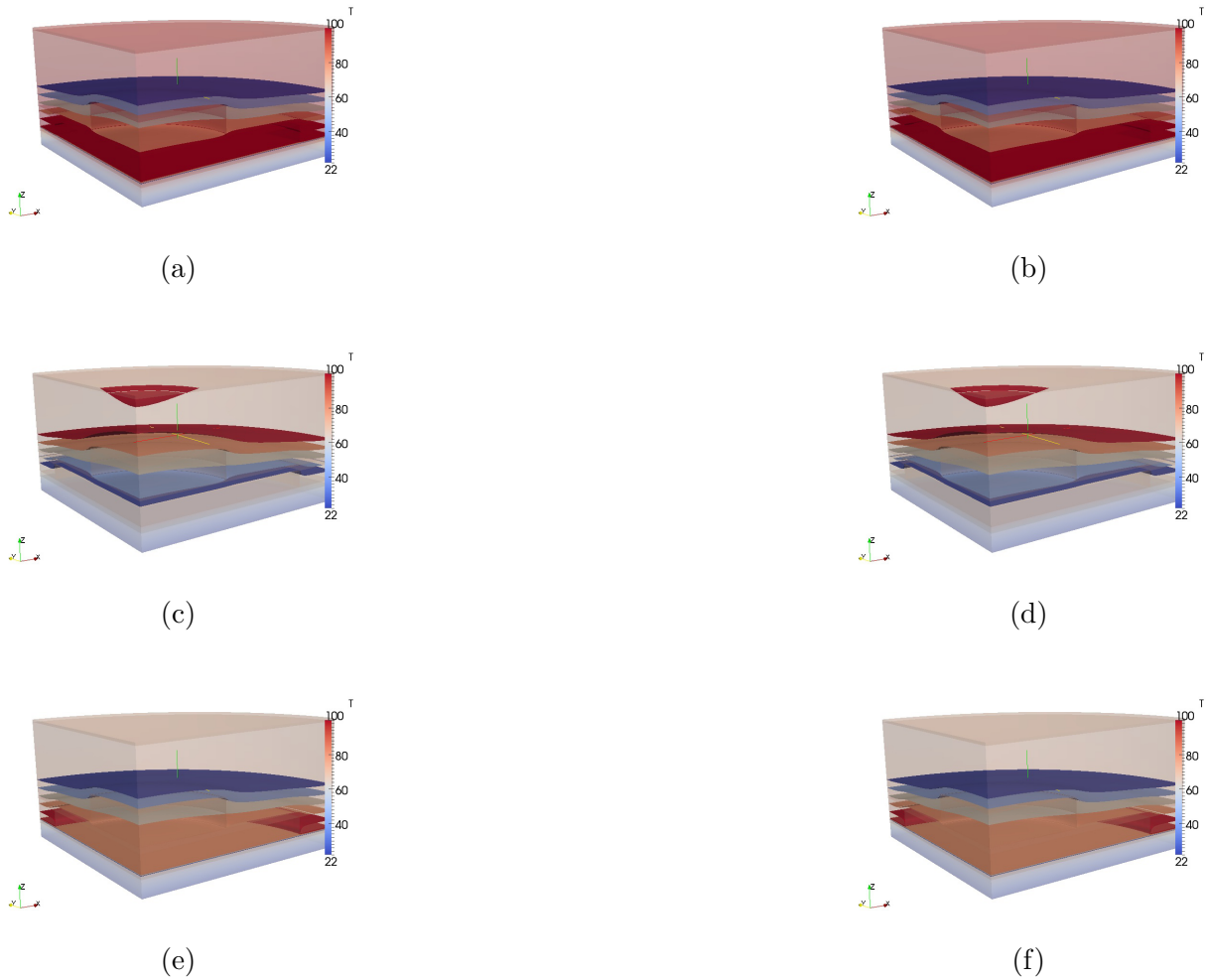
Figure 5.9: Figures show a close up of the PCR Chamber and Surrounding Regions at the Point Where the PCR Chamber Reaches the Target Temperature (a) Denaturation 1 (b) Denaturation 2 (c) Annealing 1 (d) Annealing 2 (e) Extension 1 (f) Extension 2

5.3 Conclusions

The results of this work support the use of simulation-aided design for on-chip PCR devices. Using our simulation approach we were able to generate a three dimensional temperature

profile of the prototype design. Furthermore, by replicating the controller used in experiment our simulations were able to capture transient performance.

Using this data, it was determined that thermal gradients present in vertical direction resulted in non-ideal cycling conditions. This resulted in high thermal variablity within the PCR chamber, ranging from $1.04°C$ to $1.91°C$ at steady state. Additionally, the temperature measured by the temperature probe did not accurately reflect the temperature of the PCR chamber throughout operation. Initially, the temperature readings differed by $5°C$ or more, and settled to $0.82 - 1.51°C$ above the temperature of the PCR chamber. Experimentally, it was observed that the system did successfully amplify sample DNA. However, due to the non-ideal temperature control, as described above, the output of the reactor featured a high concentration of primer-dimers.

In order to improve uniformity and temperature control within the prototype system, it is recomended that the vertical temperature gradient be reduced. This can be achieved in several ways. Additional insulation may be placed above the PCR chamber, thus increasing the thermal resistance consequently heat flow across the PCR chamber. Conversly, an additional heating element may be placed above the PCR chamber such that it mirrors the temperature of the heating element below the chamber. In this way one can compensate for the heat flow being directed across the reactor chamber. Furthermore, it is recommended that the manifold radius be increased in order to reduce the thermal gradient in the radial direction.

Chapter 6

Conclusions & Future Work

6.1   Conclusions

In this research project, simulation-based engineering was used to further understand the heat transfer properties of a microfluidic PCR device and compared with experimental analysis through collaborations. Using our simulations we were able to capture the three dimensional transient temperature profile of a microfluidic PCR device without perturbing the system with additional temperature sensors. This allowed us to understand how physical characteristics affected temperature profiles within the device. Furthermore, we were able to relate the temperature measured by collocated sensors, with that of the PCR chamber. Finally, simulation results enabled a more detailed understanding of spatial variations in temperature and heating/cooling response times for the microfluidic PCR device. The specific results from this research project were:

1. An `OpenFOAM`-based conjugate heat transfer solver which includes microfluidic PCR-specific functionality (bulk heating and PID control) was developed and verified through experimental corroboration.

2. Simulations of a prototype microfluidic PCR device with control were performed resulting in transient temperature profiles within the PCR reaction chamber.

3. Qualitative validation of the simulations was accomplished through finding that simulation deviations of PCR chamber conditions (from ideal) directly relate to observed experimental measurements of PCR device reaction products.

6.2 Recommendations

Recommendations for future work include:

1. Determine insights from simulation predictions of device performance (reaction chamber temperature uniformity and control effectiveness) for future design optimizations and "clean-sheet" re-designs of microfluidic PCR devices.

2. Validate simulation predictions of "clean-sheet" designs using experimental testing of prototypes.

3. Optimize the control system for future designs developed in silico as well as ones based on experimental analysis. This would involve optimizing PID gain parameters.

4. In this initial study we developed prototype systems where we attempted to control the effect of convection by using a sealed chamber. In future simulations, we could vary the convective heat transfer coefficient and study its effect on the temperature distribution.

References

[1] Rolfe C Anderson, Xing Su, Gregory J Bogdan, and Jeffery Fenton. A miniature integrated device for automated multistep genetic assays. *Nucleic Acids Research*, 28(12):e60–e60, 2000.

[2] U.M. Ascher and L.R. Petzold. *Computer methods for ordinary differential equations and differential-algebraic equations*. Society for Industrial Mathematics, 1998.

[3] Adrian Bejan. *Heat Transfer*. John Wiley & Sons, 1993.

[4] Phillip Belgrader, Christopher J Elkin, Steven B Brown, Shanavaz N Nasarabadi, Richard G Langlois, Fred P Milanovich, Bill W Colston, and Graham D Marshall. A reusable flow-through polymerase chain reaction instrument for the continuous monitoring of infectious biological agents. *Analytical chemistry*, 75(14):3446–3450, 2003.

[5] R.B Bird, W.E. Stewart, and E.N. Lightfoot. *Transport Phenomena*. John Wiley and Sons, New York, second edition, 2002.

[6] Cynthia J Bruckner-Lea, Toyoko Tsukuda, Brian Dockendorff, James C Follansbee, Mark T Kingsley, Cathy Ocampo, Jennie R Stults, and Darrell P Chandler. Renewable microcolumns for automated dna purification and flow-through amplification: from sediment samples through polymerase chain reaction. *Analytica Chimica Acta*, 469(1):129–140, 2002.

[7] Mark A Burns, Carlos H Mastrangelo, Timothy S Sammarco, Francis P Man, James R Webster, BN Johnsons, Bradley Foerster, Darren Jones, Yakeitha Fields, Adam R Kaiser, et al. Microfabricated structures for integrated dna analysis. *Proceedings of the National Academy of Sciences*, 93(11):5556–5561, 1996.

[8] Nathaniel C Cady, Scott Stelick, Madanagopal V Kunnavakkam, and Carl A Batt. Real-time pcr detection of listeria monocytogenes using an integrated microfluidics platform. *Sensors and Actuators B: Chemical*, 107(1):332–341, 2005.

[9] Ajit M Chaudhari, Timothy M Woudenberg, Michael Albin, and Kenneth E Goodson. Transient liquid crystal thermometry of microfabricated pcr vessel arrays. *Microelectromechanical Systems, Journal of*, 7(4):345–355, 1998.

[10] Jing Cheng, Mann A Shoffner, Georgi E Hvichia, Larry J Kricka, and Peter Wilding. Chip pcr. ii. investigation of different pcr amplification systems in microfabricated silicon-glass chips. *Nucleic Acids Research*, 24(2):380–385, 1996.

[11] Alice Chien, David B. Edgar, and John M. Trela. Deoxyribonucleic acid polymerase from the extreme thermophile thermus aquaticus. *Journal of Bacteriology*, 1976.

[12] Jeff Chiou, Paul Matsudaira, Ain Sonin, and Daniel Ehrlich. A closed-cycle capillary polymerase chain reaction machine. *Analytical chemistry*, 73(9):2018–2021, 2001.

[13] CF Chou, R Lenigk, D Sadler, R Changrani, S ORourke, R Liu, et al. Rapid genotyping with integrated continuous-flow pcr and bioelectronic detection. In *7th international conference on miniaturized chemical and biochemical analysis systems Squaw Valley, California USA*, pages 1203–5, 2003.

[14] T. J. Chung. *Computational Fluid Dynamics*. Cambridge University Press, 2002.

[15] Mario Curcio and Johan Roeraade. Continuous segmented-flow polymerase chain reaction for high-throughput miniaturized dna amplification. *Analytical chemistry*, 75(1):1–7, 2003.

[16] JH Daniel, S Iqbal, RB Millington, DF Moore, CR Lowe, DL Leslie, MA Lee, and MJ Pearce. Silicon microchambers for dna amplification. *Sensors and Actuators A: Physical*, 71(1):81–88, 1998.

[17] Manish Deshpande, Ken B Greiner, Bart F Romanowicz, John R Gilbert, Pamela M St John, and Timothy Woudenberg. Cad analysis of pcr well containment. *MSM1999, San Juan, Puerto Rico, USA*, 1999.

[18] William C Dunn, Stephen C Jacobson, Larry C Waters, Natalia Kroutchinina, Julia Khandurina, Robert S Foote, Monica J Justice, Lisa J Stubbs, and J Michael Ramsey. Pcr amplification and analysis of simple sequence length polymorphisms in mouse dna using a single microchip device. *Analytical biochemistry*, 277(1):157–160, 2000.

[19] Jamil El-Ali, Ivan R Perch-Nielsen, Claus Riber Poulsen, Dang Duong Bang, Pieter Telleman, and Anders Wolff. Simulation and experimental validation of a su-8 based pcr thermocycler chip with integrated heaters and temperature sensor. *Sensors and Actuators A: Physical*, 110(1):3–10, 2004.

[20] Enzoklop. Schematic drawing of the pcr cycle. http://en.wikipedia.org/wiki/File:Polymerase_chain_reaction.svg, April 2014.

[21] Ivan Erill, Susana Campoy, Nadina Erill, Jordi Barbé, and Jordi Aguiló. Biochemical analysis and optimization of inhibition and adsorption phenomena in glass–silicon pcr-chips. *Sensors and Actuators B: Chemical*, 96(3):685–692, 2003.

[22] Ivan Erill, Susana Campoy, José Rus, Luis Fonseca, Antoni Ivorra, Zenón Navarro, José A Plaza, Jordi Aguiló, and Jordi Barbé. Development of a cmos-compatible pcr chip: comparison of design and system strategies. *Journal of Micromechanics and Microengineering*, 14(11):1558, 2004.

[23] ZH Fan, AJ Ricco, W Tan, M Zhao, and CG Koh. Integrating multiplexed pcr with ce for detecting microorganisms. *Micro Total Anal Syst*, 849:90, 2003.

[24] Jana Felbel, Ivonne Bieber, and Johann M Koehler. Chemical surface management for micro pcr in silicon chip thermocyclers. In *SPIE's International Symposium on Smart Materials, Nano-, and Micro-Smart Systems*, pages 34–40. International Society for Optics and Photonics, 2002.

[25] Christian Fermér, Peter Nilsson, and Mats Larhed. Microwave-assisted high-speed pcr. *European journal of pharmaceutical sciences*, 18(2):129–132, 2003.

[26] Jerome P Ferrance, Qirong Wu, Braden Giordano, Casandra Hernandez, Yien Kwok, Karen Snow, Steve Thibodeau, and James P Landers. Developments toward a complete micro-total analysis system for duchenne muscular dystrophy diagnosis. *Analytica Chimica Acta*, 500(1):223–236, 2003.

[27] OpenFOAM Foundation. The openfoam foundation. http://www.openfoam.org/.

[28] David N Fredricks and David A Relman. Application of polymerase chain reaction to the diagnosis of infectious diseases. *Clinical infectious diseases*, pages 475–486, 1999.

[29] Neal A Friedman and Deirdre R Meldrum. Capillary tube resistive thermal cycling. *Analytical chemistry*, 70(14):2997–3002, 1998.

[30] Tatsuhiro Fukuba, Takeshi Naganuma, and Teruo Fujii. Microfabricated flow-through pcr device for underwater microbiological study. In *Underwater Technology, 2002. Proceedings of the 2002 International Symposium on*, pages 101–105. IEEE, 2002.

[31] Tatsuhiro Fukuba, Takatoki Yamamoto, Takeshi Naganuma, and Teruo Fujii. Micro-fabricated flow-through device for dna amplification – towards in situ gene analysis. *Chemical Engineering Journal*, 101(1):151–156, 2004.

[32] Peter Gascoyne, Jutamaad Satayavivad, and Mathuros Ruchirawat. Microfluidic approaches to malaria detection. *Acta tropica*, 89(3):357–369, 2004.

[33] BC Giordano, J Ferrance, S Swedberg, AFR Hühmer, and JP Landers. Polymerase chain reaction in polymeric microchips: Dna amplification in less than 240 seconds. *Analytical biochemistry*, 291(1):124–132, 2001.

[34] Braden C Giordano, Ebony R Copeland, and James P Landers. Towards dynamic coating of glass microchip chambers for amplifying dna via the polymerase chain reaction. *Electrophoresis*, 22(2):334–340, 2001.

[35] Bernhard Gschaider. The incomplete swak4foam reference. https://github.com/wyldckat/swak4foam/blob/master/Documentation/swak4FoamReference.org, 2013.

[36] Anja Gulliksen, Lars Solli, Frank Karlsen, Henrik Rogne, Eivind Hovig, Trine Nord-strøm, and Reidun Sirevåg. Real-time nucleic acid sequence-based amplification in nanoliter volumes. *Analytical chemistry*, 76(1):9–14, 2004.

[37] Gordon H Hall, David L Sloan, Tianchi Ma, Madeline H Couse, Stephane Martel, Duncan G Elliott, D Moira Glerum, and Christopher J Backhouse. An optical relay approach to very low cost hybrid polymer-complementary metal-oxide semiconductor electrophoresis instrumentation. *Journal of chromatography. A*, 1349:122–128, May 2014.

[38] Viet N Hoang, Govind V Kaigala, and Christopher J Backhouse. Optimization of thin film heater/sensor design for miniature devices using finite element analysis. In *COMSOL Multiphysics Users Conference*, 2005. Burlington, MA, USA (August 30, 2005).

[39] Jong Wook Hong, Teruo Fujii, Minoru Seki, Takatoki Yamamoto, and Isao Endo. Integration of gene amplification and capillary gel electrophoresis on a polydimethylsiloxane-glass hybrid microchip. *Electrophoresis*, 22(2):328–333, 2001.

[40] AFR Hühmer and JP Landers. Noncontact infrared-mediated thermocycling for effective polymerase chain reaction amplification of dna in nanoliter volumes. *Analytical chemistry*, 72(21):5507–5512, 2000.

[41] Ventzeslav P Iordanov, Jeroen Bastemeijer, Andre Bossche, Pasqualina M Sarro, Michal Malatek, Ian T Young, Gijs WK Van Dedem, and Michael J Vellekoop. Pcr array on chip-thermal characterization. In *Sensors, 2003. Proceedings of IEEE*, volume 2, pages 1045–1048. IEEE, 2003.

[42] H Jasak. *Error analysis and estimation for the Finite Volume method with applications to fluid flows.* PhD thesis, University of London, 1996.

[43] Massoud Kaviany. *Principles of Heat Transfer.* John Wiley & Sons, Inc., 2002.

[44] Julia Khandurina, Timothy E McKnight, Stephen C Jacobson, Larry C Waters, Robert S Foote, and J Michael Ramsey. Integrated system for rapid pcr-based dna analysis in microfluidic devices. *Analytical Chemistry*, 72(13):2995–3000, 2000.

[45] Chee G Koh, Woei Tan, Ming-qi Zhao, Antonio J Ricco, and Z Hugh Fan. Integrating polymerase chain reaction, valving, and electrophoresis in a plastic device for bacterial detection. *Analytical Chemistry*, 75(17):4591–4598, 2003.

[46] Martin U Kopp, Andrew J De Mello, and Andreas Manz. Chemical amplification: continuous-flow pcr on a chip. *Science*, 280(5366):1046–1048, 1998.

[47] ET Lagally, JR Scherer, RG Blazej, NM Toriello, BA Diep, M Ramchandani, GF Sensabaugh, LW Riley, and RA Mathies. Integrated portable genetic analysis microsystem for pathogen/infectious disease detection. *Analytical Chemistry*, 76(11):3162–3170, 2004.

[48] Alex IK Lao, Thomas MH Lee, I Hsing, Nancy Y Ip, et al. Precise temperature control of microfluidic chamber for gas and liquid phase reactions. *Sensors and Actuators A: Physical*, 84(1):11–17, 2000.

[49] Frances C. Lawyer, Susanne Stoffel, Randall K. Saiki, Sheng-Yung Chang, Phoebe A. Landre, Richard D. Abramson, and David H. Gelfand. High-level expression, purification, and enzymatic characterization of full-length thermus aquaticus dna polymerase and a truncated form deficient in 5' to 3' exonuclease activity. *Genome Research*, 1993.

[50] Dae-Sik Lee, SH Park, H Yang, TH Yoon, SJ Kim, H Kim, YB Shin, K Kim, and YT Kim. Submicroliter-volume pcr chip with fast thermal response and very low power consumption. In *Proc. of microTAS*, volume 2003, 2003.

[51] Chia-Sheng Liao, Gwo-Bin Lee, Jiunn-Jong Wu, Chih-Ching Chang, Tsung-Min Hsieh, Fu-Chun Huang, and Ching-Hsing Luo. Micromachined polymerase chain reaction system for multiple dna amplification of upper respiratory tract infectious diseases. *Biosensors and Bioelectronics*, 20(7):1341–1348, 2005.

[52] Yu-Cheng Lin, Chung-Che Yang, and Ming-Yuan Huang. Simulation and experimental validation of micro polymerase chain reaction chips. *Sensors and Actuators B: Chemical*, 71(1):127–133, 2000.

[53] Jian Liu, Carl Hansen, and Stephen R Quake. Solving the world-to-chip interface problem with a microfluidic matrix. *Analytical chemistry*, 75(18):4718–4723, 2003.

[54] Yasutaka Matsubara, Kagan Kerman, Masaaki Kobayashi, Shouhei Yamamura, Yasutaka Morita, and Eiichi Tamiya. Microchamber array based dna quantification and specific sequence detection from a single copy via pcr in nanoliter volumes. *Biosensors and Bioelectronics*, 20(8):1482–1490, 2005.

[55] William Messner and Dawn Tilbury. Pid controller design. http://ctms.engin.umich.edu/CTMS/index.php?example=Introduction&section=ControlPID, 2011.

[56] Hidenori Nagai, Yuji Murakami, Yasutaka Morita, Kenji Yokoyama, and Eiichi Tamiya. Development of a microchamber array for picoliter pcr. *Analytical chemistry*, 73(5):1043–1047, 2001.

[57] Hidenori Nagai, Yuji Murakami, Kenji Yokoyama, and Eiichi Tamiya. High-throughput pcr in silicon based microchamber array. *Biosensors and Bioelectronics*, 16(9):1015–1019, 2001.

[58] Jonathan Nakane, David Broemeling, Roger Donaldson, Andre Marziali, Thomas D Willis, Matthew O'Keefe, and Ronald W Davis. A method for parallel, automated, thermal cycling of submicroliter samples. *Genome research*, 11(3):441–447, 2001.

[59] M. A. Northrop, R. F. Hills, P Landre, S. Lewhew, D. Hadley, and R. Watson. A mems-based dna analysis system. In *Transducer '95 eighth international conference on solid state Sensors Actuators*, 1995.

[60] Pierre J Obeid and Theodore K Christopoulos. Continuous-flow dna and rna amplification chip combined with laser-induced fluorescence detection. *Analytica Chimica Acta*, 494(1):1–9, 2003.

[61] Pierre J Obeid, Theodore K Christopoulos, H John Crabtree, and Christopher J Backhouse. Microfabricated device for dna and rna amplification by continuous-flow polymerase chain reaction and reverse transcription-polymerase chain reaction with cycle number selection. *Analytical chemistry*, 75(2):288–295, 2003.

[62] OpenFOAM Foundation. *OpenFOAM The Open Source CFD Toolbox: Programmer's Guide*, version 2.3.0 edition, February 2014.

[63] Nokyoung Park, Suhyeon Kim, and Jong Hoon Hahn. Cylindrical compact thermal-cycling device for continuous-flow polymerase chain reaction. *Analytical chemistry*, 75(21):6029–6033, 2003.

[64] Seungkyung Park, Yi Zhang, Shin Lin, Tza-Huei Wang, and Samuel Yang. Advances in microfluidic pcr for point-of-care infectious disease diagnostics. *Biotechnology advances*, 29(6):830–839, 2011.

[65] W. Rychlik, W. J. Spencer, and R. E. Rhoads. Optimization of the annealing temperature for dna amplification in vitro. *Nucleic Acids Research*, 1990.

[66] Daniel J Sadler, Rajnish Changrani, Peter Roberts, Chia-Fu Chou, and Frederic Zenhausern. Thermal management of biomems. In *Thermal and Thermomechanical Phenomena in Electronic Systems, 2002. ITHERM 2002. The Eighth Intersociety Conference on*, pages 1025–1032. IEEE, 2002.

[67] Daniel J Sadler, Rajnish Changrani, Peter Roberts, Chia-Fu Chou, and Frederic Zenhausern. Thermal management of biomems: temperature control for ceramic-based pcr and dna detection devices. *Components and Packaging Technologies, IEEE Transactions on*, 26(2):309–316, 2003.

[68] Anita Salic, Ana Tusek, and Bruno Zelic. Application of microreactors in medicine and biomedicine. *Journal of Applied Biomedicine*, 2012.

[69] Ivonne Schneegaß, Reiner Bräutigam, and Johann Michael Köhler. Miniaturized flow-through pcr with different template types in a silicon chip thermocycler. *Lab on a Chip*, 1(1):42–49, 2001.

[70] Ivonne Schneegaß and Johann Michael Köhler. Flow-through polymerase chain reactions in chip thermocyclers. *Reviews in Molecular Biotechnology*, 82(2):101–121, 2001.

[71] Scientificdealers.com. Pcr machine. http://www.scientificdealers.com/product/PCR-Machine/26.

[72] Keyue Shen, Xiaofang Chen, Min Guo, and Jing Cheng. A microchip-based pcr device using flexible printed circuit technology. *Sensors and Actuators B: Chemical*, 105(2):251–258, 2005.

[73] Young Shik Shin, Keunchang Cho, Sun Hee Lim, Seok Chung, Sung-Jin Park, Chanil Chung, Dong-Chul Han, and Jun Keun Chang. Pdms-based micro pcr chip with parylene coating. *Journal of Micromechanics and Microengineering*, 13(5):768, 2003.

[74] Seth Stern, Carlton Brooks, Michelle Strachan, Anne Kopf-Sill, and J Wallace Parce. Microfluidic thermocyclers for genetic analysis. In *Thermal and Thermomechanical Phenomena in Electronic Systems, 2002. ITHERM 2002. The Eighth Intersociety Conference on*, pages 1033–1038. IEEE, 2002.

[75] Kai Sun, Akira Yamaguchi, Yutaka Ishida, Shigeki Matsuo, and Hiroaki Misawa. A heater-integrated transparent microchannel chip for continuous-flow pcr. *Sensors and Actuators B: Chemical*, 84(2):283–289, 2002.

[76] Theresa B Taylor, Stefanie E Harvey, Michael Albin, Lilla Lebak, Yuebin Ning, Ian Mowat, Thomas Schuerlein, and Edward Principe. Process control for optimal pcr performance in glass microstructures. *Biomedical Microdevices*, 1(1):65–70, 1998.

[77] Theresa B Taylor, Emily S Winn-Deen, Enrico Picozza, Timothy M Woudenberg, and Michael Albin. Optimization of the performance of the polymerase chain reaction in silicon-based microstructures. *Nucleic acids research*, 25(15):3164–3168, 1997.

[78] The OpenFOAM Foundation. *OpenFOAM: Open Source Field Operation and Manipulation Library*, 2014.

[79] Dieter Trau, Thomas MH Lee, Alex IK Lao, Ralf Lenigk, I-Ming Hsing, Nancy Y Ip, Maria C Carles, and Nikolaus J Sucher. Genotyping on a complementary metal oxide semiconductor silicon polymerase chain reaction chip with integrated dna microarray. *Analytical chemistry*, 74(13):3168–3173, 2002.

[80] M. W. Versteeg. *An Introduction to Computational Fluid Dynamics: The Finite Volume Method*. Pearson Prentice Hall, 2007.

[81] Nicolas von Ahsen, Carl T. Wittwer, and Ekkehard Schutz. Oligonucleotide melting temperatures under pcr conditions: Nearest-neighbor corrections for mg^{2+}, deoxynucleotide triphosphate, and dimethyl sulfoxide conectrations with comparison to alternative empirical formulas. *Molecular Diagnostics and Genetics*, 2001.

[82] Qinghui Wang and Haiqing Gong. An integrated software solution for real-time pcr analysis based on microfluidic biochip. In *Microtechnologies for the New Millennium 2003*, pages 77–86. International Society for Optics and Photonics, 2003.

[83] W Wang, ZX Li, YJ Yang, and ZY Guo. Droplet based micro oscillating flow-through pcr chip. In *Micro Electro Mechanical Systems, 2004. 17th IEEE International Conference on.(MEMS)*, pages 280–283. IEEE, 2004.

[84] Jonathan West, Boris Karamata, Brian Lillis, James P Gleeson, John Alderman, John K Collins, William Lane, Alan Mathewson, and Helen Berney. Application of magnetohydrodynamic actuation to continuous flow chemistry. *Lab on a Chip*, 2(4):224–230, 2002.

[85] Dae Sung Yoon, You-Seop Lee, Youngsun Lee, Hye Jung Cho, Su Whan Sung, Kwang W Oh, Junhoe Cha, and Geunbae Lim. Precise temperature control and rapid thermal cycling in a micromachined dna polymerase chain reaction chip. *Journal of Micromechanics and Microengineering*, 12(6):813, 2002.

[86] Xiaomei Yu, Dacheng Zhang, Ting Li, Lin Hao, and Xiuhan Li. 3-d microarrays biochip for dna amplification in polydimethylsiloxane (pdms) elastomer. *Sensors and Actuators A: physical*, 108(1):103–107, 2003.

[87] Po Ki Yuen, Larry J Kricka, Paolo Fortina, Nicholas J Panaro, Taku Sakazume, and Peter Wilding. Microchip module for blood sample preparation and nucleic acid amplification reactions. *Genome Research*, 11(3):405–412, 2001.

[88] Chunsun Zhang, Jinliang Xu, Wenli Ma, and Wenling Zheng. Pcr microfluidic devices for dna amplification. *Biotechnology advances*, 24(3):243–284, 2006.

[89] Nanyan Zhang, Hongdong Tan, and Edward S Yeung. Automated and integrated system for high-throughput dna genotyping directly from blood. *Analytical chemistry*, 71(6):1138–1145, 1999.

[90] TH Zhang, K Chakrabarty, and RB Fair. System performance evaluation with system c for two pcr microelectrofluidic systems. In *Technical Proc. 2002 Int. Conf. on Modeling and Simulation of Microsystems (San Juan, Puerto Rico, USA, 22–25 April)*, pages 48–53, 2002.

[91] Zhan Zhao, Dafu Cui, Zhongyao Yu, Li Wang, Shanhong Xia, and Zheng Cui. Heat properties of an integrated micro pcr vessel. In *International Conference on Sensing units and Sensor Technology*, pages 31–34. International Society for Optics and Photonics, 2001.

[92] Quanbo Zou, Yubo Miao, Yu Chen, Uppili Sridhar, Chong Ser Chong, Taichong Chai, Yan Tie, Christina Hui Leng Teh, Tit Meng Lim, and ChewKiat Heng. Micro-assembled multi-chamber thermal cycler for low-cost reaction chip thermal multiplexing. *Sensors and Actuators A: Physical*, 102(1):114–121, 2002.

[93] Quanbo Zou, Uppili Sridhar, Yu Chen, and Janak Singh. Miniaturized independently controllable multichamber thermal cycler. *Sensors Journal, IEEE*, 3(6):774–780, 2003.